

Classical Cepheid pulsation models. VI. The Hertzsprung progression

G. Bono¹, M. Marconi², and R. F. Stellingwerf³

¹ Osservatorio Astronomico di Roma, Via Frascati 33, 00040 Monte Porzio Catone, Italy; bono@coma.mporzio.astro.it

² Osservatorio Astronomico di Capodimonte, Via Moiariello 16, 80131 Napoli, Italy; marcella@na.astro.it

³ SC, 2229 Loma Linda, Los Alamos, NM 87544, USA; rfs@stellingwerf.com

the date of receipt and acceptance should be inserted later

Abstract. We present the results of an extensive theoretical investigation on the pulsation behavior of Bump Cepheids. We constructed several sequences of full amplitude, nonlinear, convective models by adopting a chemical composition typical of Large Magellanic Cloud (LMC) Cepheids ($Y=0.25$, $Z=0.008$) and stellar masses ranging from $M/M_{\odot}=6.55$ to 7.45. We find that theoretical light and velocity curves reproduce the HP, and indeed close to the blue edge the bump is located along the descending branch, toward longer periods it crosses at first the luminosity/velocity maximum and then it appears along the rising branch. In particular, we find that the predicted period at the HP center is $P_{\text{HP}} = 11.24 \pm 0.46$ d and that such a value is in very good agreement with the empirical value estimated by adopting the Fourier parameters of LMC Cepheid light curves i.e. $P_{\text{HP}} = 11.2 \pm 0.8$ d (Welch et al. 1997). Moreover, light and velocity amplitudes present a "double-peaked" distribution which is in good qualitative agreement with observational evidence on Bump Cepheids. It turns out that both the skewness and the acuteness typically show a well-defined minimum at the HP center and the periods range from $P_{\text{HP}} = 10.73 \pm 0.97$ d to $P_{\text{HP}} = 11.29 \pm 0.53$ d which are in good agreement with empirical estimates. We also find that the models at the HP center are located within the resonance region but not on the 2:1 resonance line ($P_2/P_0 = 0.5$), and indeed the P_2/P_0 ratios roughly range from 0.51 (cool models) to 0.52 (hot models).

Interestingly enough, the predicted Bump Cepheid masses, based on a Mass-Luminosity (ML) relation which neglects the convective core overshooting, are in good agreement with the empirical masses of Galactic Cepheids estimated by adopting the Baade-Wesselink method (Gieren 1989). As a matter of fact, the observed mass at the HP center $-P \approx 11.2$ d- is $6.9 \pm 0.9 M_{\odot}$, while the predicted mass is $7.0 \pm 0.45 M_{\odot}$. Even by accounting for the metallicity difference between Galactic and

LMC Cepheids, this result seems to settle down the long-standing problem of the Bump mass discrepancy.

Finally, the dynamical behavior of a cool Bump Cepheid model provides a plain explanation of an ill-understood empirical evidence. In fact, it turns out that toward cooler effective temperatures the bump becomes the main maximum, while the true maximum is the bump which appears along the rising branch. This finding also supplies a plain explanation of the reason why the pulsation amplitudes of Bump Cepheids present a "double-peaked" distribution.

Key words: Stars: variables: Cepheids – hydrodynamics – Magellanic Clouds – stars: distances – stars: evolution – stars: oscillations

1. INTRODUCTION

More than seventy years ago Hertzsprung (1926) discovered that a subsample of Galactic classical Cepheids presents a relationship between the bump along the light curve and the pulsation period; the so-called "Hertzsprung Progression" was subsequently discovered among Magellanic Clouds (MCs) and Andromeda Cepheids by Kukarkin & Parenago (1937), Shapley & Mckibben Nail (1940), and by Payne-Gaposchkin (1951,1954). The HP observational scenario was enriched by Joy (1937) and by Ledoux & Walraven (1958) who found a similar behavior in radial velocity curves.

The empirical finger-print of the HP is the following: classical Cepheids in the period range $6 < P < 16$ d show a bump along both the light and the velocity curves. This secondary feature appears on the descending branch of the light curve for Cepheids with periods up to 9 days, while it appears close to maximum light for $9 < P < 12$ d and moves at earlier phases for longer periods. On the basis of this observational evidence this group of variables was christened "Bump Cepheids" for avoiding to be mixed-up with "Beat Cepheids". In fact, the latter group refer to mixed-mode variables -i.e. objects in which two

or more modes are simultaneously excited- and therefore both the shape of the light curves and the pulsation amplitudes change from one cycle to the next, whereas Bump Cepheids are single mode variables and their pulsation properties are characterized by a strong regularity over consecutive cycles.

A more quantitative approach concerning Bump Cepheids was originally suggested by Kukarkin & Parenago (1937), Payne-Gaposchkin (1947), and more recently by Simon & Lee (1981) who investigated the shape of the light curves by means of Fourier analysis. The last authors found that both the phase difference $-\phi_{21}$ - and the amplitude ratio $-R_{21}$ - show a sharp minimum close to the HP center. Following this approach several investigations have been already devoted to Fourier parameters of Galactic and Magellanic Cepheids. In particular, Moskalik et al. (1992, hereinafter MBM) suggested that the minimum in the Fourier parameters for Galactic Cepheids takes place at $P_{\text{HP}} = 10.0 \pm 0.5$ d, while Moskalik et al. (2000) by investigating a sample of more than 100 radial velocity curves found $P_{\text{HP}} = 9.95 \pm 0.05$ d. At the same time, Welch et al. (1997) by investigating a large sample of Cepheids in the LMC estimated that the minimum in the Fourier parameters is located at $P_{\text{HP}} = 11.2 \pm 0.8$ d. Thus supporting the shift of the HP center toward longer periods originally suggested by Payne-Gaposchkin (1951) and strengthened by Andreasen & Petersen (1987) and by Andreasen (1988). More recently Beaulieu (1998) suggested that the HP center in LMC and in Small Magellanic Cloud (SMC) Cepheids is located at $P_{\text{HP}} = 10.5 \pm 0.5$ d and $P_{\text{HP}} = 11.0 \pm 0.5$ d respectively. Since these three stellar systems are characterized by different mean metallicities, namely $Z=0.02$ (Galaxy), $Z=0.008$ (LMC), and $Z=0.004$ (SMC), this empirical evidence seems to suggest that a decrease in metallicity moves the HP center toward longer periods.

Up to now, two distinct models have been proposed in the literature to explain the appearance of the HP among Bump Cepheids; the *echo model* and the *resonance model*. The former was suggested by Whitney (1956) and discussed by Christy (1968,1975) on the basis of Cepheid nonlinear, radiative models. According to Christy, during each cycle close to the phases of minimum radius and before the phase of maximum expansion velocity a pressure excess is generated in the first He ionization region. This pressure excess causes a rapid expansion which in turn generates two pressure waves moving outward and inward. The latter reaches the stellar core close to the phase of maximum radius, then reflects and reaches the surface one cycle later causing the appearance of the bump. The *resonance model* was suggested by Simon & Schmidt (1976, hereinafter SS) and is based on linear, adiabatic periods. In this theoretical framework the bump would be caused by a resonance between the second overtone and the fundamental mode and it takes place when the period ratio between these two modes is close to 0.5. In particular, they suggested

that the instability of the fundamental mode drives, due to a resonance, the second overtone instability. This explanation lies on the evidence that the nonlinear, radiative models constructed by Stobie (1969) show a bump along the radial velocity curves close to the resonance line $P_2/P_0 = 0.5$.

Such an extensive observational and theoretical effort devoted to Bump Cepheids were not only aimed at understanding the HP but also at providing independent estimates of both the mass and the radius of these variables. In fact, dating back to Christy (1968, 1975), Stobie (1969) and Fricke et al. (1972, hereinafter FSS) it was suggested that these two evolutionary parameters can be constrained on the basis of period and phase of the bump. A different method to estimate the mass, based on period ratios, was suggested by Petersen (1973). Note that mass determinations based on these two methods present a compelling feature: they are based on observables such as periods and phases of the bump which are not affected by systematic empirical uncertainties and therefore they are only limited by photometric accuracy. However, pulsational masses based on these methods are, with few exceptions (Carson & Stothers 1988, hereinafter CS), systematically smaller than the evolutionary masses. This longstanding puzzle raised the so-called Bump mass discrepancy (see also Cox 1980) and at the same time supported the use of a ML relation based on evolutionary models which include a mild or a strong convective core overshooting (Simon 1995; Wood 1998). Even though, the new radiative opacities settled down this *vexata questio* (MBM; Kanbur & Simon 1994; Simon & Kanbur 1994, hereinafter SK), recent linear (Buchler et al. 1996; Simon & Young 1997) and nonlinear (Wood et al. 1997) predictions for Cepheids in the MCs present a small discrepancy with the ML relations predicted by current evolutionary models.

The main aim of this paper is to use up-to-date nonlinear hydrodynamical models which include the coupling between pulsation and convection as well as canonical evolutionary masses, to account for the observed properties of Bump Cepheids. In this investigation we focus our attention on the classical HP and refer to a forthcoming investigation (Bono et al. in preparation) a more detailed discussion on the physical mechanisms which trigger the appearance of the HP among Bump Cepheids and on other resonances recently proposed for both short (Antonello & Poretti 1986; Buchler et al. 1996) and long-period Cepheids (Pel 1978; Antonello 1998). In order to supply a detailed theoretical scenario we constructed a fine grid of full amplitude, nonlinear, convective models by adopting stellar masses ranging from 6.4 to $7.6 M_{\odot}$ and a fixed chemical composition, namely $Y=0.25$, $Z=0.008$. We adopted this chemical composition, because accurate observational data on LMC Cepheids are currently available in the literature. At the same time, this metal abundance can supply useful constraints on the intrinsic accu-

racy of our nonlinear models, and indeed recent nonlinear, Cepheid models constructed by adopting similar treatments of the coupling between pulsation and convection show at intermediate metal contents very large pulsation destabilizations and it has been suggested that a powerful dissipation mechanism was not properly included in current pulsation codes (Buchler 2000).

In §2 we briefly recall the theoretical framework adopted for constructing Cepheid models and present nonlinear observables predicted by these models as well as their light and velocity curves. The systematic behavior of both luminosity and velocity amplitudes inside the instability strip is investigated in §3. In this section we also present the skewness and the acuteness of light and velocity curves and discuss the use of these parameters to mark the position of the HP center. New analytical relations which connect the period at the HP center to the stellar mass and to the effective temperature of Bump Cepheid models at minimum amplitude are also provided in this section. In §4 we discuss the location of these models in the HR diagram, and compare the HP center predicted by nonlinear models with linear and nonlinear resonance lines. The dynamical behavior of two Bump Cepheid models located close to the HP center and to the red edge of the instability strip is investigated in detail in sect. 5. The main results of this investigation are summarized in §6 together with a brief discussion on the observables which can supply tight constraints on the accuracy of theoretical models.

2. Theoretical framework

The theoretical framework adopted for constructing full amplitude, nonlinear, convective Cepheid models was already described in Bono et al. (1998) and in paper I (Bono et al. 1999) and therefore it is not discussed further here. The reader interested in the physical assumptions adopted to account for the coupling between pulsation and convection is referred to Buchler (2000). In paper III (Bono et al. in preparation) we found that the sequence of models constructed by assuming $M/M_{\odot}=7.0$ and $Y=0.25$, $Z=0.008$ showed a bump along both light and velocity curves which appears at earlier pulsation phases when moving toward longer periods. Accordingly, the amplitudes of these models showed a "double-peaked" distribution with the two maxima located close to the blue (hot) and to the red (cool) edge of the instability strip and a well-defined minimum close to $P \approx 10.7$ d. On the basis of these features we concluded that this sequence of models undergoes the HP when moving from the blue to the red edge. A similar behavior in the distribution of radial velocity amplitudes was also found by CS in a nonlinear, radiative investigation of Bump Cepheid models. However as noted by the same authors, the velocity amplitudes were systematically larger than the observed ones and the predicted periods at the HP center were 10% longer than expected.

In order to supply a more detailed mapping of the HP inside the instability strip we implemented the sequence at $M/M_{\odot}=7.0$ with new series of models constructed by adopting a mass step of $0.15 M_{\odot}$. Linear and nonlinear calculations were performed by adopting the same input physics (opacity, equation of state) and the same ML relation adopted in our previous investigations and based on evolutionary models which neglect the convective core overshooting (see paper I and III for more details). The new sequences were extended in mass until we found a well-defined minimum in the pulsation amplitudes inside the instability strip. For providing a robust relationship between the bump progression and the pulsation period we adopted a temperature step of 100 K throughout the instability strip and of only 50 K where the bump crosses the luminosity maximum and moves from the descending to the rising branch. We end up with six new series of models ranging in mass from 6.55 to $7.45 M_{\odot}$ which show the typical behavior of the HP. After the initial perturbation of the static model (see paper I) the approach to the nonlinear limit cycle required a direct time integration ranging from 1500 to 5000 cycles.

The input parameters of each sequence are listed in Table 1. This table gives the nonlinear pulsation properties of the models which present a stable limit cycle. We typically adopted a temperature step of 100 K, therefore the edges of the instability region can be estimated by increasing/decreasing the effective temperature of the hottest/coolest model by 50 K. The first three columns list for each model the stellar mass (solar units), the logarithmic luminosity (solar units), and the static effective temperature (K). Columns 4) and 5) give the nonlinear, fundamental period (d) and the logarithmic mean radius (solar units). The observables listed in the other columns are the following: 6) fractional radius oscillation, i.e. $\Delta R/R_{\text{ph}} = (R^{\text{max}} - R^{\text{min}})/R_{\text{ph}}$ where R_{ph} is the photospheric radius; 7) radial velocity amplitude (km s^{-1}), i.e. $\Delta u = u^{\text{max}} - u^{\text{min}}$; 8) bolometric amplitude (mag), i.e. $\Delta M_{\text{bol}} = M_{\text{bol}}^{\text{max}} - M_{\text{bol}}^{\text{min}}$; 9) logarithmic amplitude of static gravity, i.e. $\Delta \log g_s = \log g_s^{\text{max}} - \log g_s^{\text{min}}$; 10) logarithmic amplitude of effective gravity, i.e. $\Delta \log g_{\text{eff}} = \log g_{\text{eff}}^{\text{max}} - \log g_{\text{eff}}^{\text{min}}$ where $g_{\text{eff}} = GM/R^2 + du/dt$; 11) temperature amplitude (K), i.e. $\Delta T = T^{\text{max}} - T^{\text{min}}$ where T is the temperature of the outer boundary; 12) effective temperature amplitude (K), i.e. $\Delta T_e = T_e^{\text{max}} - T_e^{\text{min}}$ where T_e is derived from the surface luminosity, 13) total Kinetic energy (erg). The quantities listed in columns 4) to 11) refer, with the exception of the effective gravity, to the surface zone.

Figs. 1-6, show the light and the velocity curves of the six new sequences for the labeled values of both mass and luminosities. Light and velocity curves of the sequence for $M/M_{\odot}=7.0$ were already published in the ApJ on-line edition of paper III (Fig. 11f). Note that light and velocity curves plotted in these figures show neither spurious secondary features (bumps or dips) along the pulsation

cycle nor sudden jumps close to the phases of maximum compression. As already noted in paper I and III, this feature is a significative improvement in comparison with light and velocity curves predicted by nonlinear, radiative models (Christy 1975), and indeed theoretical curves were plotted without applying any running average or filtering process for smoothing the surface variations (Karp 1975). This finding is even more relevant for investigating the HP. In fact, up to now nonlinear, radiative predictions were mainly based on radial velocity curves, since the light curves presented several spurious secondary features (CS; MBM). As a consequence, even though the bulk of observational data on the HP comes from light curves, theoretical insights were focused on the shape of radial velocity curves.

Curves displayed in Figs. 1-6 show quite clearly that when moving from hotter to cooler effective temperatures the bump moves from the descending branch to the rising branch, i.e. an increase in the period moves the bump along the transition: descending branch \rightarrow luminosity maximum \rightarrow rising branch. Theoretical predictions in Figs. 1-6 disclose two key features:

a) the bump along the light curves crosses the luminosity maximum at shorter periods when compared with the velocity curves. This means that at fixed mass and for decreasing effective temperatures the Cepheid light curves start to show a flat-topped shape when the velocity curves still present the bump along the descending branch. This finding suggests that the lasting of the flat-topped phase in the luminosity curve is mainly governed by radius rather than by temperature variations.

b) Along each sequence the model which attains the smallest velocity amplitude presents a flat-topped shape and the minimum in the luminosity amplitude coincides, within current temperature resolution, with the minimum in the velocity amplitude. On the basis of this evidence we will assume as period of the HP center - P_{HP} - the period of the model which attains, along each sequence, the minimum amplitude in both luminosity and velocity changes.

3. HP Systematic behavior

In order to provide a quantitative estimate of the change in the pulsation properties we take into account three different parameters, namely the amplitude, the acuteness, and the skewness of both light and velocity curves. Although the Fourier parameters supply more detailed information on the dynamical behavior along the pulsation cycle, we adopted these three parameters because we are mainly interested in the HP center and also because they can be safely estimated even if the light and the velocity curves are not perfectly sampled.

According to Stellingwerf & Donohoe (1987) we define the acuteness as the ratio of the phase duration during which the magnitude is fainter than the median magnitude $-m_{\text{med}} = 0.5 * (m_{\text{max}} + m_{\text{min}})$ - to the phase du-

ration during which it is brighter $-\phi_b$ - than m_{med} , i.e. $Ac = (1/\phi_b) - 1$. This quantity is a measure of the top-down asymmetry of the light curve and it decreases when the shape changes from sawtooth to flat-topped. At the same time, we define the skewness as the ratio of the phase duration of the descending branch to the phase duration of the rising branch $-\phi_r$, i.e. $Sk = (1/\phi_r) - 1$. This quantity is a measure of the asymmetry between rising and decreasing branch and it decreases when the slope of the rising branch becomes flatter. For symmetrical curves -not necessarily sinusoidal- both Sk and Ac attain values close to 1.

Table 2 gives in the first two columns the mass and the effective temperature of each model, and in column 3) the ratio of second overtone to fundamental period. Since the second overtones are pulsationally stable in this region of the instability strip, we adopted for this mode the linear, nonadiabatic period. Columns 4) to 6) list the amplitude, the acuteness and the skewness of visual light curves. Bolometric magnitudes were transformed into V magnitudes by adopting bolometric corrections by Castelli et al. (1997). Columns 7) and 8) give the acuteness and the skewness of radial velocity curves.

Fig. 7 shows the luminosity amplitude in the V band $-Av$ - (top panel), the skewness (middle panel), and the acuteness (bottom panel) as a function of the logarithmic period. Sequences characterized by different stellar masses (see labeled values) are plotted using different symbols. Data plotted in Fig. 7 show that these three parameters typically present well-defined minima. We find that an increase in the stellar mass moves these minima toward longer periods and that the periods of these minima are located at $P_{\text{HP}}(Av) = 11.24 \pm 0.46$ d, $P_{\text{HP}}(Ac) = 11.17 \pm 0.48$ d, and $P_{\text{HP}}(Sk) = 10.73 \pm 0.97$ d, where the errors give the standard deviations. The period of the HP center based on Sk minima is shorter than $P_{\text{HP}}(Av)$, and $P_{\text{HP}}(Ac)$ because the sequence for $M/M_{\odot} = 6.55$ does not show a sharp minimum.

These theoretical minima appear in very good agreement with the empirical determination based on the Fourier parameters ϕ_{21} and R_{21} of a large sample of LMC Cepheids provided by Welch et al. (1997) i.e. $P_{\text{HP}} = 11.2 \pm 0.8$ d and in reasonable agreement with the estimate, based on the same approach, provided by Beaulieu (1998) i.e. $P_{\text{HP}} = 10.5 \pm 0.5$ d. Here we note that the observed P_{HP} value was estimated as the period at which the Fourier parameters ϕ_{21} and R_{21} of the light curves present a sudden jump, while the predicted P_{HP} values are the periods at which Bump Cepheid models attain the minimum value in Av , Sk , and Ac respectively. However, Stellingwerf & Donohoe (1986) using adiabatic, one-zone pulsation models showed that the jump in the ϕ_{21} parameter is correlated with a local minimum in the Sk parameter. At the same time, Andreasen & Petersen (1987) in a detailed analysis of both amplitudes and Fourier parameters found that the jump in ϕ_{21} and in R_{21} of LMC Bump Cepheids

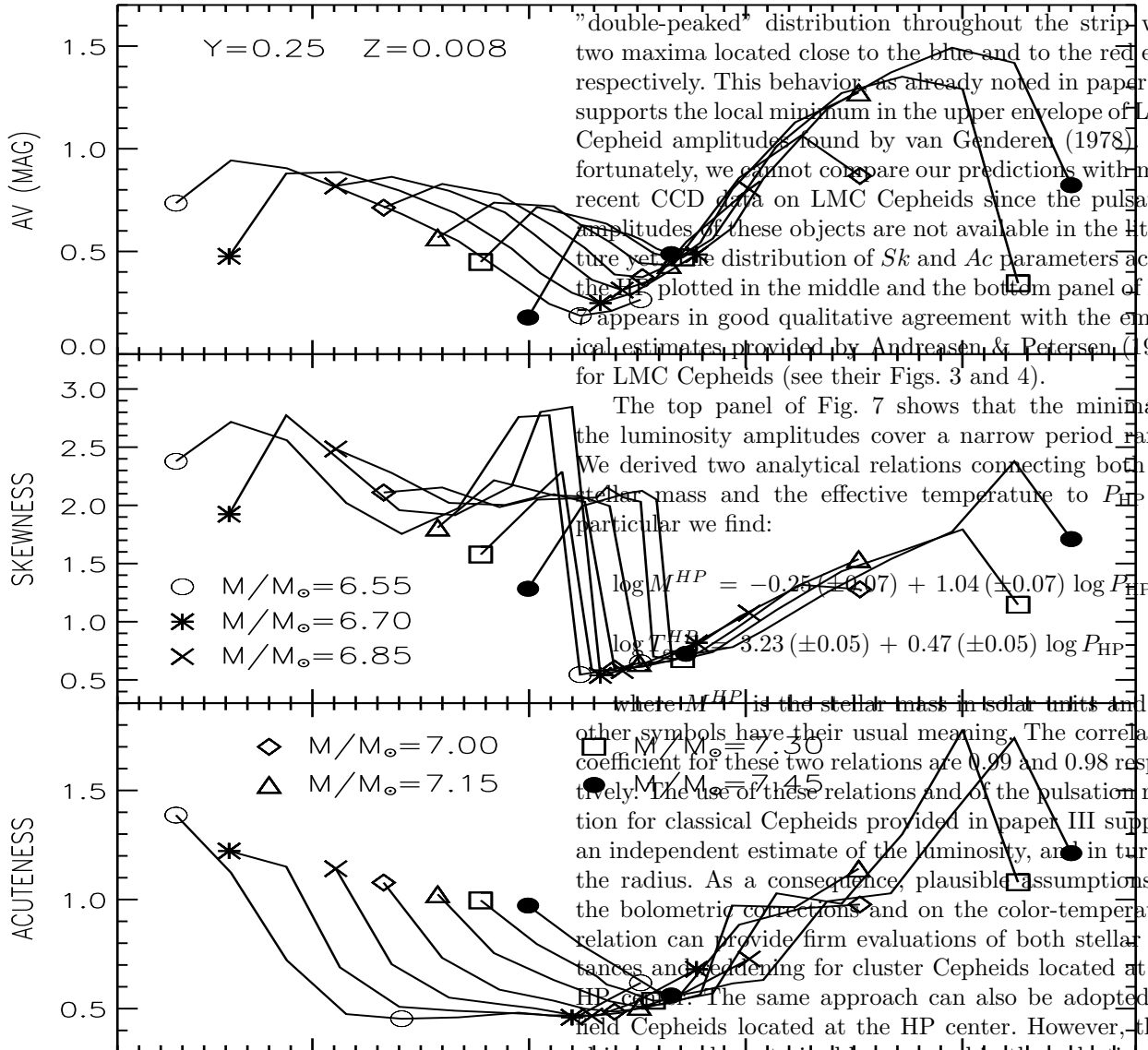


Fig. 7. Luminosity amplitude in the V band (top panel), skewness (middle panel), and acuteness (bottom panel) as a function of logarithmic period. Models characterized by different stellar masses (see labeled values) were plotted using different symbols.

takes place at the same period, within observational uncertainties, at which the B photographic amplitudes, the skewness, and the acuteness attain their minimum value. As a consequence, we conclude that not only $P_{\text{HP}}(AV)$ but also $P_{\text{HP}}(Sk)$ and $P_{\text{HP}}(Ac)$ are robust indicators of the HP center.

Data plotted in the top panel show that when moving from the blue to the red edge the luminosity amplitudes do not show a monotonic behavior with stellar mass. In fact, close to the blue edge an increase in the stellar mass causes a decrease in the pulsation amplitudes, whereas close to the red edge the amplitudes present an opposite behavior. Moreover, the luminosity amplitudes present a

"double-peaked" distribution throughout the strip with two maxima located close to the blue and to the red edge respectively. This behavior was already noted in paper III, supports the local minimum in the upper envelope of LMC Cepheid amplitudes found by van Genderen (1978). Unfortunately, we cannot compare our predictions with more recent CCD data on LMC Cepheids since the pulsation amplitudes of these objects are not available in the literature yet. The distribution of Sk and Ac parameters across the HP plotted in the middle and the bottom panel of Fig. 7 appears in good qualitative agreement with the empirical estimates provided by Andreadsen & Petersen (1987) for LMC Cepheids (see their Figs. 3 and 4).

The top panel of Fig. 7 shows that the minima in the luminosity amplitudes cover a narrow period range. We derived two analytical relations connecting both the stellar mass and the effective temperature to P_{HP} . In particular we find:

$$\log M^{HP} = -0.25 (\pm 0.07) + 1.04 (\pm 0.07) \log P_{\text{HP}}$$

$$\log T_e^{HP} = 3.23 (\pm 0.05) + 0.47 (\pm 0.05) \log P_{\text{HP}}$$

where M^{HP} is the stellar mass in solar units and the other symbols have their usual meaning. The correlation coefficient for these two relations are 0.99 and 0.98 respectively. The use of these relations and of the pulsation relation for classical Cepheids provided in paper III supplies an independent estimate of the luminosity, and in turn of the radius. As a consequence, plausible assumptions on the bolometric corrections and on the color-temperature relation can provide firm evaluations of both stellar distances and scaling for cluster Cepheids located at the HP center. The same approach can also be adopted for field Cepheids located at the HP center. However, these objects are characterized by a spread in the pulsation period and therefore the masses and the effective temperatures derived using the previous relations can be affected by larger uncertainties. In fact, by adopting the empirical value $P_{\text{HP}} = 11.2 \pm 0.8$ d provided by Welch et al. (1997) we find $M^{HP} = 7.0 \pm 1.0 M_{\odot}$, and $T_e^{HP} = 5300 \pm 600$ K.

Fig. 8 shows the same parameters of Fig. 7 but for the radial velocity curves. The behavior of ΔV , Sk , and Ac versus period are quite similar to the behaviors of the same parameters of the light curves. We find that the periods of the minima are now located at $P_{\text{HP}}(\Delta V) = 11.24 \pm 0.46$ d, $P_{\text{HP}}(Ac) = 11.29 \pm 0.53$ d, and $P_{\text{HP}}(Sk) = 11.27 \pm 0.49$ d respectively, and are once again in good agreement with empirical estimates. Although light and velocity curves show quite similar Sk values over the whole period range, the velocity curves present larger Sk values just before the HP center. This effect is due to the fact that the shape of the velocity curves becomes flat-topped at minimum amplitude whereas the light curves show the same shape at shorter periods (see §2). The comparison of predicted radial velocity amplitudes with observational data is dif-

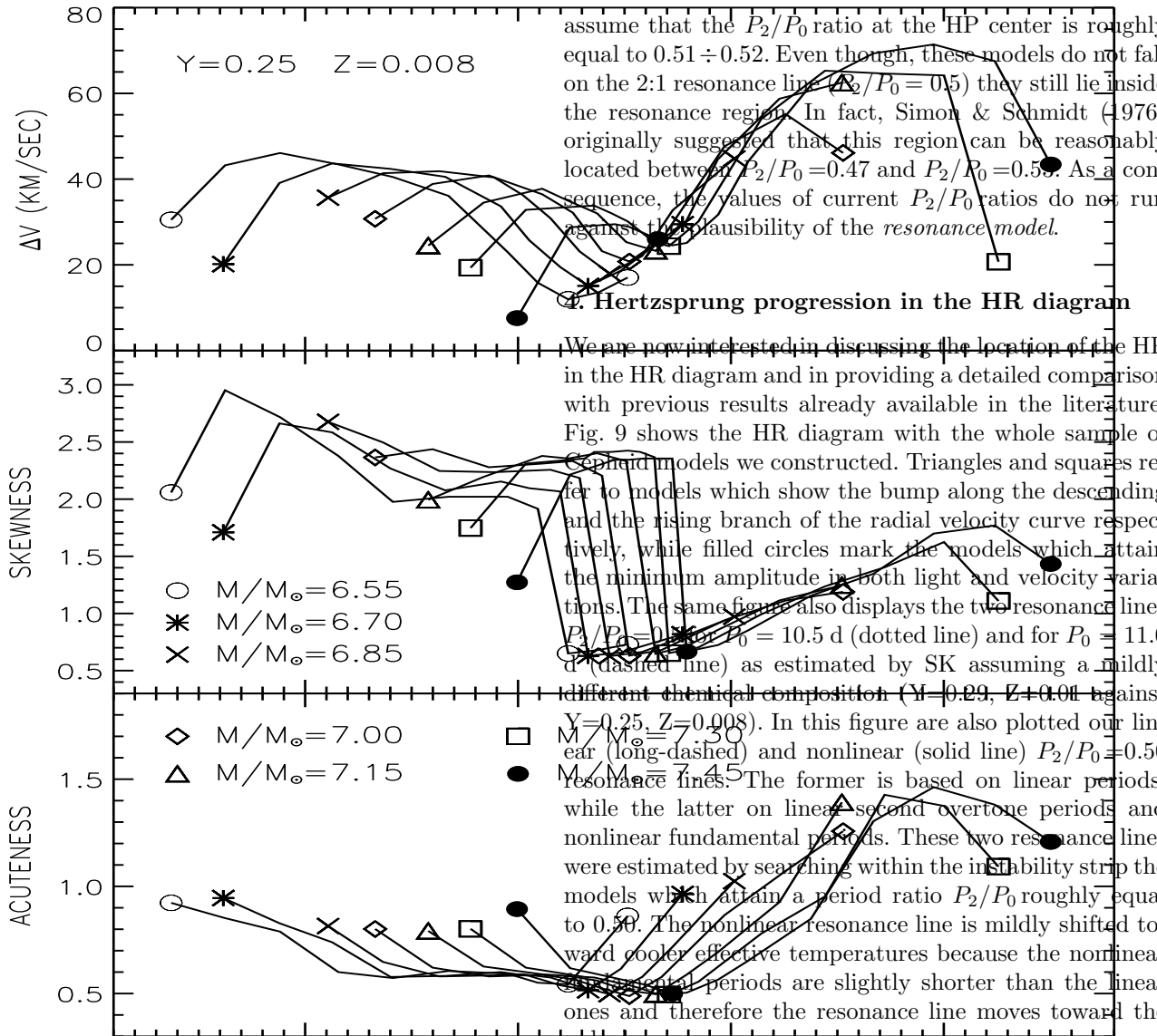


Fig. 8. Similar to Fig. 7, but for the radial velocity curves (see text for more details).

ficult since spectroscopic measurement of LMC Cepheids are very scanty or do not cover the HP (Antonello 1998). However, radial velocity amplitudes for Galactic Cepheids (see Fig. 9 of paper III) collected by Cogan (1980) and by Bersier et al. (1994) show that the upper envelope presents a well-defined minimum across the HP center. The same outcome applies to the skewness, and indeed recent spectroscopic measurements of Galactic Cepheids (Gorynya 1998) show a sharp decrease close to $\log P \approx 1$. This provides a qualitative support to the predicted minima and to the "double-peaked" distributions shown in Fig. 8.

Finally, we note that the P_2/P_0 ratios (see Table 2) of the models located at the HP center range from 0.517 for the $M/M_\odot = 6.55$ model to 0.512 for the $M/M_\odot = 7.45$ model. These period ratios were estimated by adopting the linear second overtone periods, therefore we can safely

assume that the P_2/P_0 ratio at the HP center is roughly equal to $0.51 \div 0.52$. Even though, these models do not fall on the 2:1 resonance line ($P_2/P_0 = 0.5$) they still lie inside the resonance region. In fact, Simon & Schmidt (1976) originally suggested that this region can be reasonably located between $P_2/P_0 = 0.47$ and $P_2/P_0 = 0.55$. As a consequence, the values of current P_2/P_0 ratios do not run against the plausibility of the *resonance model*.

4. Hertzsprung progression in the HR diagram

We are now interested in discussing the location of the HP in the HR diagram and in providing a detailed comparison with previous results already available in the literature. Fig. 9 shows the HR diagram with the whole sample of Cepheid models we constructed. Triangles and squares refer to models which show the bump along the descending and the rising branch of the radial velocity curve respectively, while filled circles mark the models which attain the minimum amplitude in both light and velocity variations. The same figure also displays the two resonance lines $P_2/P_0 = 0.5$ for $P_0 = 10.5$ d (dotted line) and for $P_0 = 11.0$ d (dashed line) as estimated by SK assuming a mildly different chemical composition ($Y=0.29$, $Z=0.01$) against $Y=0.25$, $Z=0.008$. In this figure are also plotted our linear (long-dashed) and nonlinear (solid line) $P_2/P_0 = 0.50$ $M/M_\odot = 7.30$ and $M/M_\odot = 7.45$ resonance lines. The former is based on linear periods, while the latter on linear second overtone periods and nonlinear fundamental periods. These two resonance lines were estimated by searching within the instability strip the models which attain a period ratio P_2/P_0 roughly equal to 0.50. The nonlinear resonance line is mildly shifted toward cooler effective temperatures because the nonlinear fundamental periods are slightly shorter than the linear ones and therefore the resonance line moves toward the red edge.

The SK resonance lines were evaluated by adopting a Newton-Raphson algorithm which for each given value of the effective temperature constructs a sequence of linear, nonadiabatic, radiative models by iterating on the values of mass and luminosity until both the resonance condition $-P_2/P_0 = 0.5$ and the resonance center $-P_0 = 10.5, 11.0$ d are matched. A slightly different approach for estimating the resonance lines in a linear regime was suggested by Buchler et al. (1996) but their predictions were not included in Fig. 9, because the effective temperature values were not provided.

Fig. 9 shows that the SK resonance lines are located at hotter effective temperatures when compared with the nonlinear HP centers and this discrepancy increases toward higher luminosities. On the other hand, our linear and nonlinear resonance lines are located at effective temperatures systematically cooler than the nonlinear HP centers. The difference between our and SK resonance lines is not surprising, since our pulsation models are constructed by adopting different physical assumptions and chemical

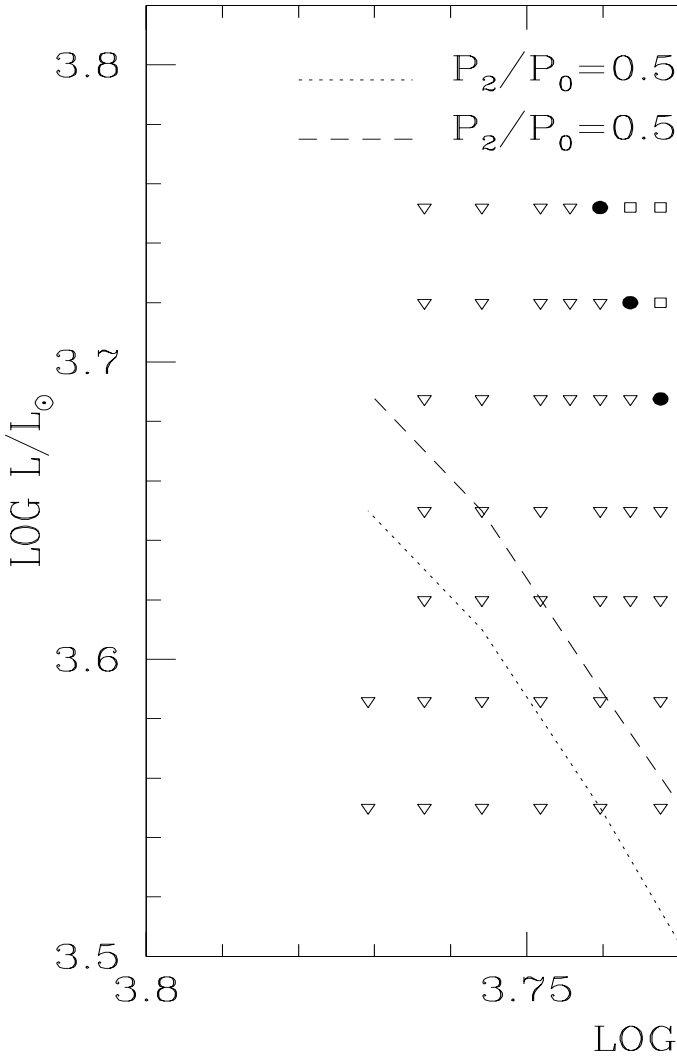


Fig. 9. Distribution in the HR diagram of Bump Cepheid models. Cepheid models with a bump along the descending or the rising branch are plotted as triangles and squares. Cepheid models which attain along each sequence the minimum amplitude are plotted as filled circles. The dotted and the dashed lines refer to the linear $P_2/P_0 = 0.5$ resonance lines derived by SK assuming that the resonance center is at $P_0 = 10.5$ d and 11.0 d respectively. The long-dashed and the solid lines show our linear and nonlinear $P_2/P_0 = 0.50$ resonance lines.

composition. However, we note that for each given luminosity the stellar masses adopted by SK are systematically smaller than our mass values and this difference typically increases when moving from lower to higher luminosities.

The same difference appears in mass estimates, based on a similar approach, provided by Beaulieu & Sasselov (1997, and references therein), and indeed for LMC Bump Cepheids at the resonance center $P_0 = 10.5$ d they give a

mass value of $4.57 M_\odot$. In order to test how the dynamical behavior depends on stellar mass, we constructed a new full amplitude, fundamental model by adopting the input parameters ($M/M_\odot = 5.35$, $\log L/L_\odot = 3.65$, $T_\text{eff} = 5700$ K) and chemical composition ($Y=0.29$, $Z=0.01$) used by SK. We selected this model since its location in the HR diagram is coincident with a model of our sequence for $M/M_\odot = 7.0$ ($\log L/L_\odot = 3.65$, $T_\text{eff} = 5700$ K). Fig. 10 shows light (top) and velocity (bottom) curves as a function of phase for our model (solid lines) and the model constructed by adopting the SK parameters (dashed lines). Although, the two models attain similar pulsation amplitudes (see Table 3) the shape of the curves is quite different. In fact, the bump in the less-massive model is located along the rising branch, while in the more-massive model along the descending branch.

However, the key result disclosed by Fig. 10 is that the the less-massive model, which is located very close to the 2:1 resonance line ($P_2/P_0 \approx 0.494$, $P_0 = 11.0398$ d) presents almost symmetric curves and a small bump on the rising branch, whereas the curves of the canonical model are more asymmetric around the maximum and show a well-defined bump along the decreasing branch. This means that the previous models should present quite different Fourier parameters. On the basis of these findings we can draw the following conclusion: theoretical light and velocity curves of Bump Cepheid models depend on the adopted ML relation, therefore the comparison between theory and observations can supply independent constraints on this relation (Wood et al. 1997; paper I). Bump Cepheid models located at the HP center can provide tight constraints on theory, since the shape of light and velocity curves shows a stronger dependence on input parameters.

In this context it is noteworthy that stellar masses based on linear period ratios are, as already noted by MBM, SK, and by Buchler et al. (1996), systematically smaller than the observed ones. On the other hand, our nonlinear, convective models based on a canonical ML relation agree with empirical Galactic Cepheid masses estimated by Gieren (1989) using the Baade-Wesselink method. In fact, by using the Gieren's Period-Mass relation (his relation 2) for $P_{\text{HP}} = 11.2$ d we obtain an empirical Cepheid mass of $M/M_\odot = 6.9 \pm 0.9$. This mass value is in satisfactory agreement, within the observational uncertainties, with nonlinear predictions, and indeed at the same period the theoretical masses range from 6.55 to $7.45 M_\odot$. We know that we are comparing theoretical predictions for LMC Cepheids with observational data for Galactic Cepheids. However, current uncertainties on mass determinations are probably larger than the metallicity effect on Cepheid masses. In fact, preliminary theoretical results support the evidence that the Bump Cepheid masses at solar chemical composition are of the order of $6.5 \pm 0.25 M_\odot$ (Ricci 1999).

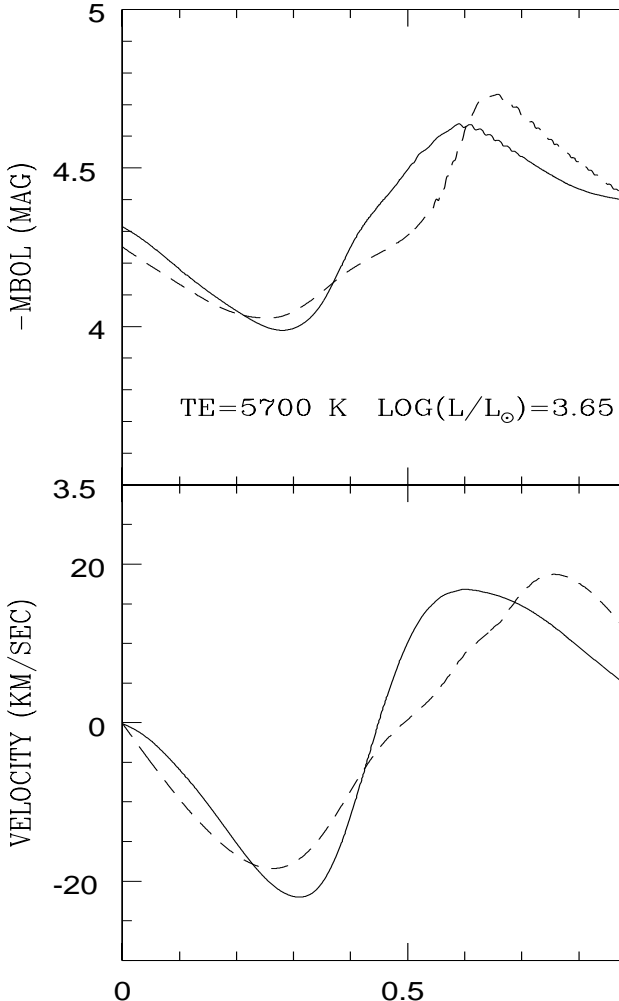


Fig. 10. Light (top panel) and velocity (bottom panel) variations along two consecutive cycles. Solid and dashed lines refer to fundamental models constructed by adopting the same luminosity and effective temperature but different composition and mass value.

As a result, predictions based on nonlinear, convective models and on canonical evolutionary tracks settle down the long-standing conundrum of the Bump mass discrepancy. However a firm conclusion on this problem can be reached as soon as pulsation calculations constructed by adopting a noncanonical ML relation (i.e. based on evolutionary models which account for convective core overshooting) will become available. Note that accurate and homogeneous mass determinations based on the near-infrared surface brightness technique (Gieren et al. 1997) and on the infrared flux method (Fernley et al. 1989) can supply tight constraints on the Cepheid ML relation. Independent mass estimates can also be derived from orbits of

Cepheids in binary systems. Interestingly enough, Evans et al. (1998) have recently observed with HST the hot binary companion of U Aql, a Galactic Bump Cepheid, and obtained for this variable a mass value of $5.1 \pm 0.7 M_{\odot}$. Taken at face value this mass estimate is roughly 20% smaller than the predicted mass range of Galactic Bump Cepheids previously mentioned. Unfortunately, up to now this is the only measurement of a Bump mass in a binary system and we still lack a firm evaluation of the error budget involved in these measurements (see their Table 2). In this context it is worth mentioning the direct measurements of Cepheid diameters through optical interferometry recently provided by Nordgren et al. (2000). As soon as $M/M_{\odot} = 5.35$, $V = 0.29$, $Z = 0.01$ data will become available, this approach can certainly supply an independent constraint on Bump Cepheid masses and in particular on the systematic uncertainties affecting empirical mass determinations.

5. Dynamical behavior of Bump Cepheid models

The appearance of the bump on the light curve is governed by temperature and radius variations. However, we focus our attention on radial velocity changes, since this is the observable generally adopted to investigate the intimate nature of the HP. In particular, we discuss the dynamical behavior of two models located at the HP center and close to red edge, the systematics of the thermal structure will be addressed in a forthcoming paper (Bono et al. in preparation).

Fig. 11 shows in a 3D plot the velocity variations as a function of mean radius and phase for a fundamental model located close to the HP center ($P_2/P_0 = 0.516$, $T = 5400$ K) of the sequence at $M/M_{\odot} = 7.0$. Regions in which the radial velocity attains positive/negative values are plotted as solid/dotted lines. For avoiding misleading interpretations of the amplitude variations the radial velocities were plotted, according to Aikawa & Whitney (1985), without applying any artificial shift or enhancement.

Data plotted in Fig. 11 show that the outermost layers contract on a shorter time scale than the regions located just below them. In fact, the external layers reach the minimum contraction velocity at $\phi = 0.23$ and then at $\phi = 0.40$ -the phase of minimum radius- start to expand, whereas the underlying regions are still contracting. We measure phases with respect to the beginning of the surface contraction at maximum radius i.e. $\phi(R = R_{\max}) = 0$. Soon after this phase the outermost layers undergo at first a rapid expansion reaching the maximum expansion velocity at $\phi = 0.54$ and then a decrease in the radial velocity due to gravity. During this slow down phase $-\phi \approx 0.65$ the outermost layers interact with deeper layers (see the arrow) that are rapidly moving outward and reach their maximum expansion velocity at $\phi \approx 0.74$. The interaction between these two different dynamical behaviors causes

an increase in the acceleration both toward the surface and toward the center. As a consequence in the outermost layers the radial velocity increases once again and then slows down showing a secondary maximum -the bump- at $\phi = 0.85$.

The innermost layers start to expand around $\phi = 0.45$ but their expansion is not in phase with the outermost layers. In fact, the latter ones reach the maximum expansion velocity at phases during which the bulk of the envelope is still accelerating. This phase difference causes the formation of a shock between the slowing down motion of outermost layers and the outgoing expansion of deeper layers. As a consequence, the shocked region undergoes a strong compression which in turn generates pressure waves that propagate both toward the surface and toward the center of the stellar model. It is the outgoing pressure wave that causes, as already noted, the appearance of the bump, whereas the incoming pressure wave -the *Christy wave*- causes a short contraction phase in the innermost regions lasting from $\phi = 0.7$ to $\phi = 0.85$. Soon after the bounce at the stellar core at $\phi = 0.95$, the *Christy wave* at first moves rapidly outward and shortly delays the beginning of the contraction phase in the innermost regions and then limits the inward excursion of the layers crossed during its propagation out to the surface. This effect causes close to the phases of minimum radius a bounce between the overlying layers -that are rapidly contracting- and these layers that are contracting more slowly. The shock formed by this bounce generates two pressure waves: the outgoing wave delays the outward excursion of the region located just below the outermost layers, while the incoming wave triggers the *Christy wave*. As a consequence, it is the propagation out to surface of the *Christy wave* generated in the previous cycle that eventually causes the phase shift between the outermost layers and of the underlying regions, and in turn the appearance of the bump.

A phase shift between the outermost layers and the bulk of the envelope was also noted by Karp (1975). However, he found that the *Christy wave* approaches the surface close to velocity maximum and not close to the bump phase, and therefore the *echo model* could not completely explain the HP. Our results support the timing suggested by Karp but it seems that it is the *Christy wave* which causes the phase shift, and in turn the bump. However, before a firm conclusion on the plausibility of this mechanism can be reached a detailed comparison between theoretical predictions and empirical data has to be provided.

We now briefly discuss the dynamical behavior of a model located close to the red edge ($P_2/P_0 = 0.502$, $T_e = 5100$ K) of the sequence at $M/M_\odot = 7.0$, since it presents an interesting feature worth being investigated. Fig. 12 shows the radial velocity as viewed from the stellar surface. The overall behavior is similar to the model located close to the HP center, but in this red model the formation and the incoming propagation of the *Christy wave* can be more easily identified. In fact, close to $\phi \approx 0.5$ and

$\log < R > / 10^{12} \approx 3.5$ its appearance is marked by a narrow region in which the velocity attains negative values and then moves inward reaching the base of the envelope at $\phi \approx 0.8$ (see the arrows). In this model the contraction of the overlying layers is more rapid than for the model close to the HP center, and indeed the *Christy wave* stops the expansion of the underlying layers. This fact and the evidence that the outermost layers start to expand at later phases causes the appearance along the surface velocity curve of a shoulder close to $\phi = 0.5 \div 0.55$ (see the arrow at the top of the envelope). Soon after these layers experience a rapid outgoing acceleration and this motion is almost in phase with the motion of the envelope and therefore the outermost layers do not interfere with the underlying regions since they are almost co-moving. It turns out that in this model the bump, i.e. what we defined as the secondary maximum, is the main maximum while the true maximum is the bump which appears on the rising branch.

This finding provides a straightforward explanation to what has been defined by FSS as *a happy but also ill-understood circumstance*. In fact, these authors in order to derive a linear relationship between period, phase of the bump and Bump Cepheid radii noted that from an observational point of view it could not be firmly stated whether the primary or the secondary maximum was generated by the *Christy wave*. To overcome this thorny problem they suggested to measure the phase of the secondary maximum if the bump is located along the descending branch and the phase of the primary maximum if the bump appears along the rising branch. The dynamical behavior of the Bump Cepheid model located close to the red edge supplies a plain theoretical support to this far-sighted observational choice. At the same time, current models also explain why light and velocity amplitudes show a "double-peaked" distribution when moving from the blue to the red edge of the instability strip. The maximum located close to the blue edge is typical of relatively short-period Cepheids (see paper III), whereas the second one is caused by the HP.

6. Summary and conclusions

This paper presents the results of an extensive theoretical investigation on Bump Cepheids. In order to provide a detailed analysis of the pulsation behavior of these objects we computed several sequences of full amplitude, nonlinear, convective models at fixed chemical composition ($Y=0.25$, $Z=0.008$). The models were constructed by adopting a mass step of $0.15M_\odot$ and a temperature step of 100 K close to the instability edges and of 50 K close to the HP center. The main outcomes of this analysis are the following:

- 1) theoretical light and velocity curves account for the HP, and indeed close to the blue edge the bump is located along the descending branch, at longer periods it crosses at

first the luminosity/velocity maximum and then appears along the rising branch.

2) In a very narrow period range both light and velocity curves show a flat-topped shape and their amplitudes attain a well-defined minimum. The predicted period of the minima $-P_{\text{HP}} = 11.24 \pm 0.46$ d- is in very good agreement with the empirical value found by Welch et al. (1997) for LMC Cepheids i.e. $P_{\text{HP}} = 11.2 \pm 0.8$ d. Moreover, light and velocity amplitudes present a "double-peaked" distribution which agrees with observational data.

3) Both the skewness and the acuteness of light and velocity curves show a well-defined minimum at the HP center and their distributions are in good qualitative agreement with empirical estimates provided by Andreasen & Petersen (1987). The periods of the HP center are, within the uncertainties, in good agreement with observational values.

4) *The models at the HP center are located within the resonance region but not on the 2:1 resonance line ($P_2/P_0 = 0.5$), and indeed the P_2/P_0 ratios range from 0.51 to 0.52.*

5) Predicted Bump Cepheid masses, based on a ML relation which neglects the convective core overshooting, are in good agreement with the empirical masses of Galactic Cepheids estimated by adopting the Baade-Wesselink method (Gieren 1989). In fact, the observed mass range at the HP center $-P = 11.2$ d- is $6.9 \pm 0.9 M_{\odot}$, while the theoretical one is $7.0 \pm 0.45 M_{\odot}$. Even if Galactic Cepheids are more metal-rich than LMC Cepheids, this result seems to settle down the long-standing problem of the Bump mass discrepancy.

The results presented in this paper were mainly aimed at testing whether current hydrodynamical models which include the coupling between pulsation and convection together with a ML relation based on canonical evolutionary models account for the HP in LMC Cepheids. It is clear that the theoretical scenario we developed seems to provide a reliable description of several empirical facts. Moreover, we confirm that Bump Cepheid models can supply fundamental constraints on stellar masses, and in turn on the ML relation of intermediate-mass stars. We also note that current Cepheid metal-intermediate, convective models do show plausible pulsation properties.

Two crucial topics need to be properly addressed before firm conclusions on the HP can be reached. To validate present nonlinear Cepheid models a thorough theoretical analysis of the Fourier parameters should be provided together with a detailed comparison with observational data available in the literature (Bono et al. in preparation). At the same time, the dependence of the HP behavior both on the chemical composition should be investigated as well. New and accurate CCD data on light and velocity amplitudes as well as on the skewness and the acuteness of these curves can certainly improve the location of the HP center and feed the future investigations with robust observational constraints.

Acknowledgements. It is a pleasure to thank V. Castellani and F. Caputo for a detailed reading of an early draft of this paper and for many interesting and enlightening discussions on Cepheids. We wish also to acknowledge N. Remage Evans and T. Nordgren for insightful discussions on current empirical estimates of Cepheid masses. We also acknowledge an anonymous referee for some useful suggestions that improved the readability of the paper.

References

Aikawa T., Whitney C. A. 1985, ApJ 296, 165
 Andreasen G. K. 1988, A&A 196, 159
 Andreasen G. K., Petersen J. O., 1987, A&A 180, 129
 Antonello E. 1998, in A Half Century of Stellar Pulsation Interpretations: a Tribute to A.N. Cox, ed. P.A. Bradley & J.A. Guzik (San Francisco: ASP), 243
 Antonello E., Poretti E., 1986, A&A 169, 149
 Beaulieu J. P. 1998, Mem. Soc. Astron. Italiana 69, 21
 Beaulieu J. P., Sasselov D. D. 1997, in Variable Stars and the Astrophysical Returns of Microlensing Surveys, ed. R. Ferlet, J.P. Maillard & B. Raban, (Editions Frontières: Gif-sur-Yvette Cedex), 193
 Bersier D., Burki G., Mayor M., Duquennoy A. 1994, A&AS 108, 25
 Bono G., Caputo F., Marconi M. 1998, ApJ 497, L43
 Bono G., Marconi M., Stellingwerf R. F. 1999, ApJS 122, 167 (paper I)
 Bono G., Castellani V., Marconi M. 2000, ApJ 529, 293 (paper III)
 Buchler J. R. 2000, in IAU Coll. 176, The Impact of Large-Scale Surveys on Pulsating Star Research, ed. L. Szabados & D. Kurtz (San Francisco: ASP), in press
 Buchler J. R., Kollath Z., Beaulieu J. P., Goupil M. J. 1996, ApJ 462, L83
 Carson R. T., Stothers R. B. 1988, ApJ 328, 196 (CS)
 Castelli F., Gratton R. G., Kurucz R. L. 1997, A&A 324, 432
 Christy R. F. 1968, Quart. J.R.A.S. 9, 13
 Christy R. F. 1975, in Cepheid Modeling, eds. D. Fischel, & W.M. Sparks, (Washington: NASA SP-383), 85
 Cogan B. C. 1980, ApJ 239, 941
 Cox A. N. 1980, ARA&A 18, 15
 Evans N. R., Boehm-Vitense E., Carpenter K., Beck-Winchatz B., Robinson R. 1998, ApJ 494, 768
 Fernley J. A., Skillen I., Jameson R. F. 1989, MNRAS 237, 947
 Fricke K., Stobie R. S., Strittmatter P. A. 1972, ApJ 171, 593 (FSS)
 Gieren W. P. 1989, A&A 225, 381
 Gieren W. P., Fouque P., Gomez M. 1997, ApJ 488, 74
 Gorynya N. A. 1998, IBVS, 4636
 Hertzsprung E. 1926, Bull. astronom. Inst. Netherl. 3, 115
 Joy A. H. 1937, ApJ 86, 363
 Kanbur S. M., Simon N. R. 1994, ApJ 420, 880
 Karp A. H. 1975, ApJ 199, 448
 Kukarkin B. V., Parenago P. P. 1937, Astronom. USSR. 14, 181
 Ledoux P., Walraven Th. 1958, in Handbuch der Physik, 51, 353
 Moskalik P., Buchler R., Marom A. 1992, ApJ 385, 685 (MBM)

Moskalik P., Krzyt T., Gorynya N. A., Samus N. N. 2000, in IAU Coll. 176, The Impact of Large-Scale Surveys on Pulsating Star Research, ed. L. Szabados & D. Kurtz (San Francisco: ASP), in press

Nordgren T. E., Armstrong J. T., Hajian A. R., Germain M. E. 2000, in IAU Coll. 176, The Impact of Large-Scale Surveys on Pulsating Star Research, ed. L. Szabados & D. Kurtz (San Francisco: ASP), in press

Payne-Gaposchkin C. 1947, AJ 52, 218

Payne-Gaposchkin C. 1951, in *Astrophysics: A Topical Symposium*, ed. J.A. Hynek (New York: McGraw Hill), 495

Payne-Gaposchkin C. 1954, Harvard Ann. 113, 153

Pel J. W. 1978, A&A 62, 75

Petersen J. O. 1973, A&A 27, 89

Ricci M. 1999, Degree Thesis, Dept. of Physics Univ. of Pisa

Shapley H., Mckibben Nail V., 1940, Proc. Nat. Acad. Sci. U.S.A. 26, 105

Simon N. R. 1995, in *Astrophysical Applications of Powerful New Databases*, ed. S.J. Adelman & W.L. Wiese, (ASP: San Francisco), 211

Simon N. R., Kanbur S. M. 1994, ApJ 429, 772 (SK)

Simon N. R., Lee A. S. 1981, ApJ 248, 291

Simon N. R., Schmidt E. G. 1976, ApJ 205, 162

Simon N. R., Young T. S. 1997, MNRAS 288, 267

Stellingwerf R. F., Donohoe M. 1986, ApJ 306, 183

Stellingwerf R. F., Donohoe M. 1987, ApJ 314, 252

Stobie R. S. 1969, MNRAS 144, 511

van Genderen A. M. 1978, A&A 65, 147

Welch D. L., Alcock C., Allsman R.A. et al. 1997, in *Variable Stars and the Astrophysical Returns of Microlensing Surveys*, ed. R. Ferlet, J.P. Maillard & B. Raban, (Editions Frontières: Gif-sur-Yvette Cedex), 205

Whitney C. A. 1956, AJ 61, 192

Wood P. R. 1998, Mem. Soc. Astron. Italiana 69, 99

Wood P. R., Arnold A., Sebo K. M. 1997, ApJ 485, L25

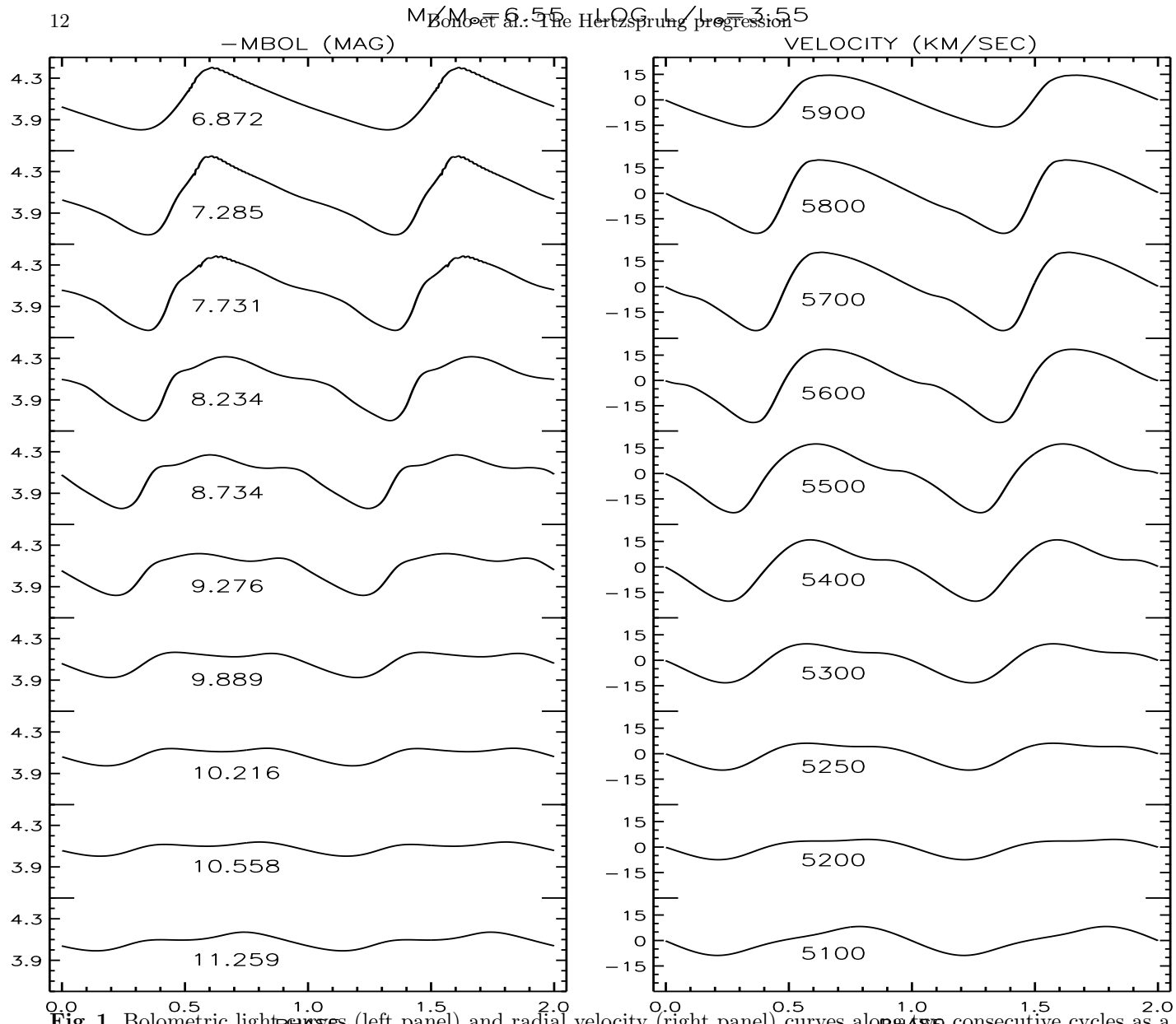


Fig. 1. Bolometric light curves (left panel) and radial velocity (right panel) curves along the Hertzsprung progression consecutive cycles as a function of the pulsation phase. The curves plotted in this figure refer to a selection of models constructed at fixed mass and luminosity (see labeled values). The nonlinear periods (d), and the effective temperatures (K) are listed in left and right panels. Positive and negative values denote expansion and contraction phases, respectively.

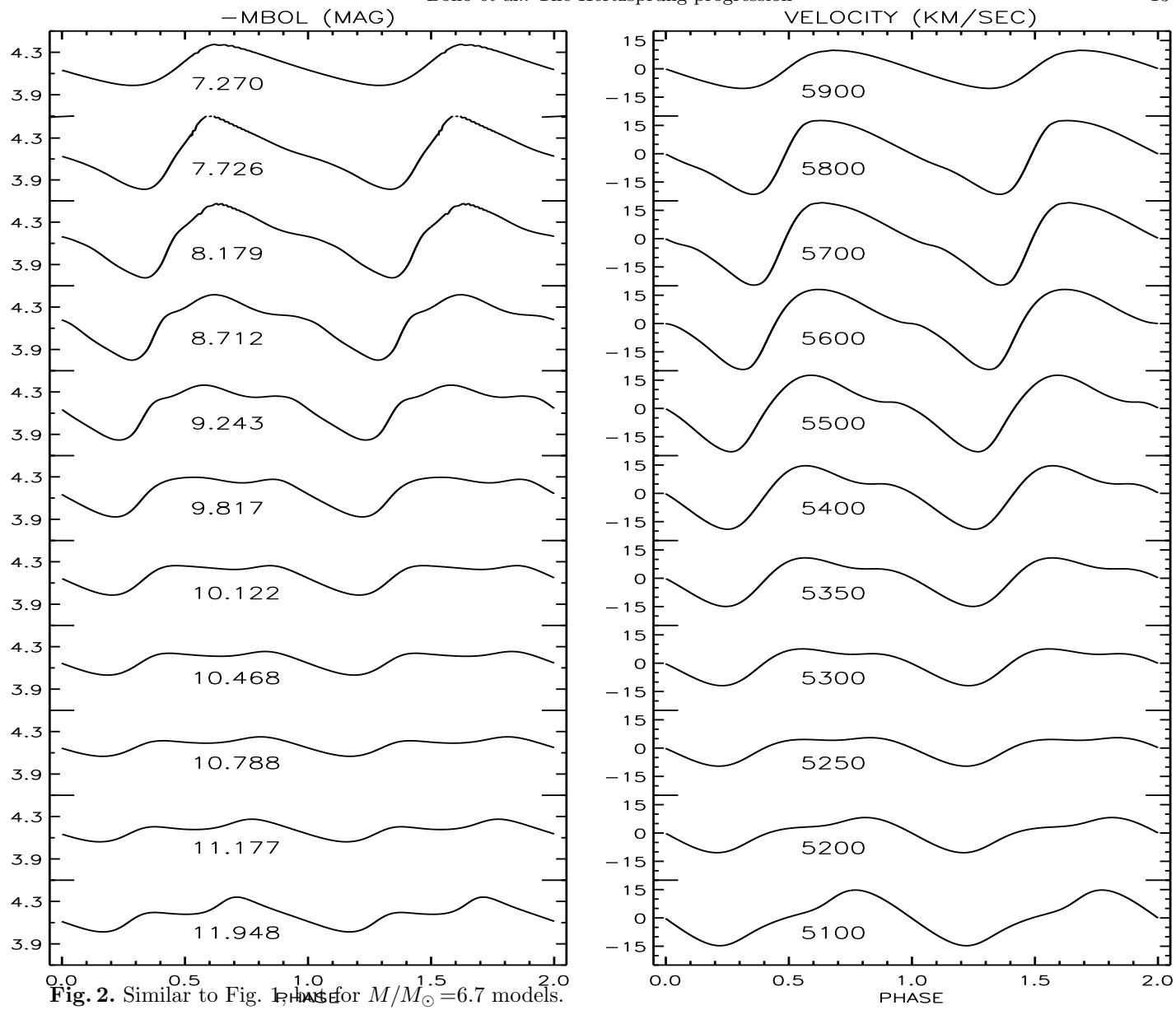
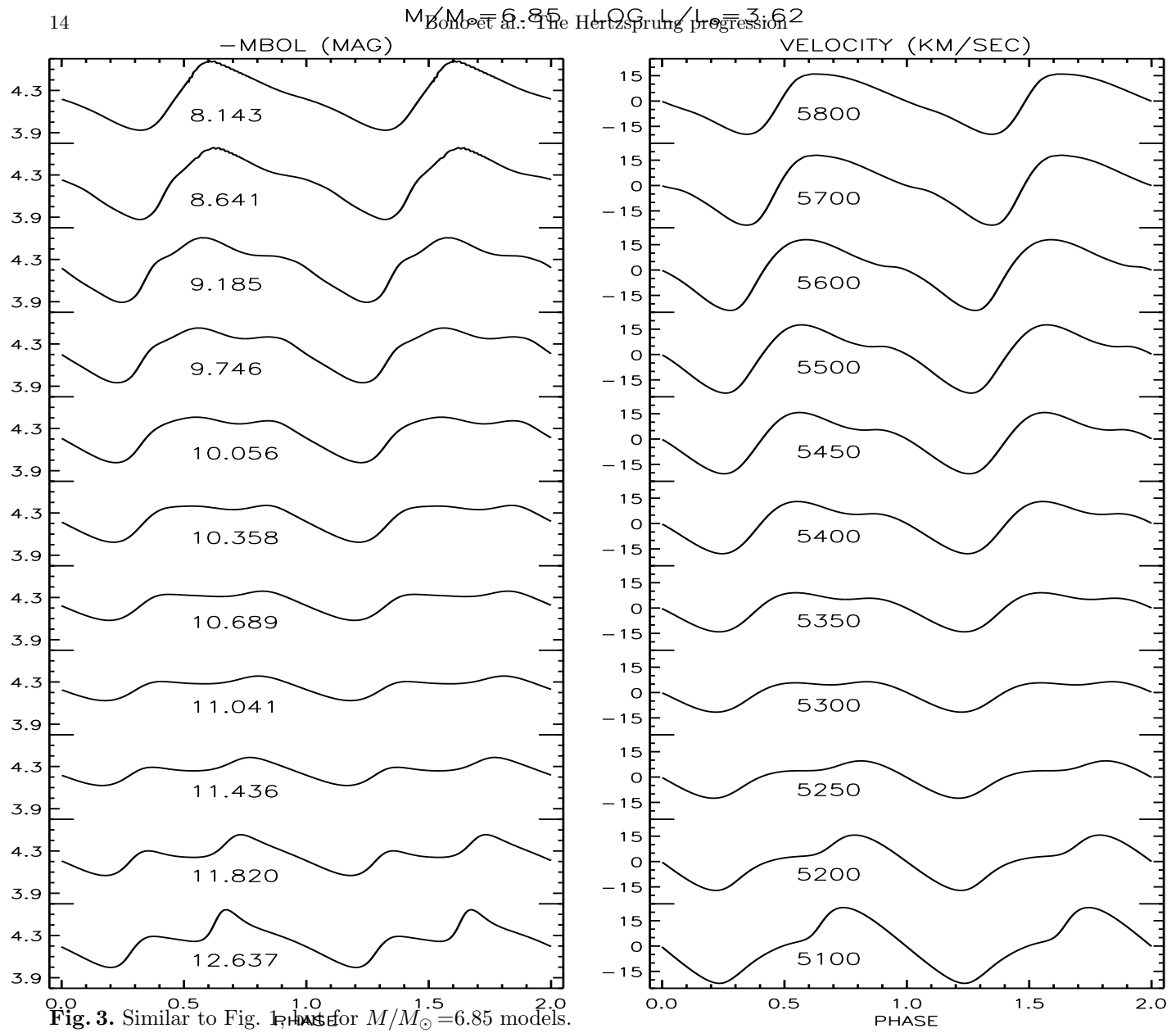


Fig. 2. Similar to Fig. 1, but for $M/M_{\odot} = 6.7$ models.



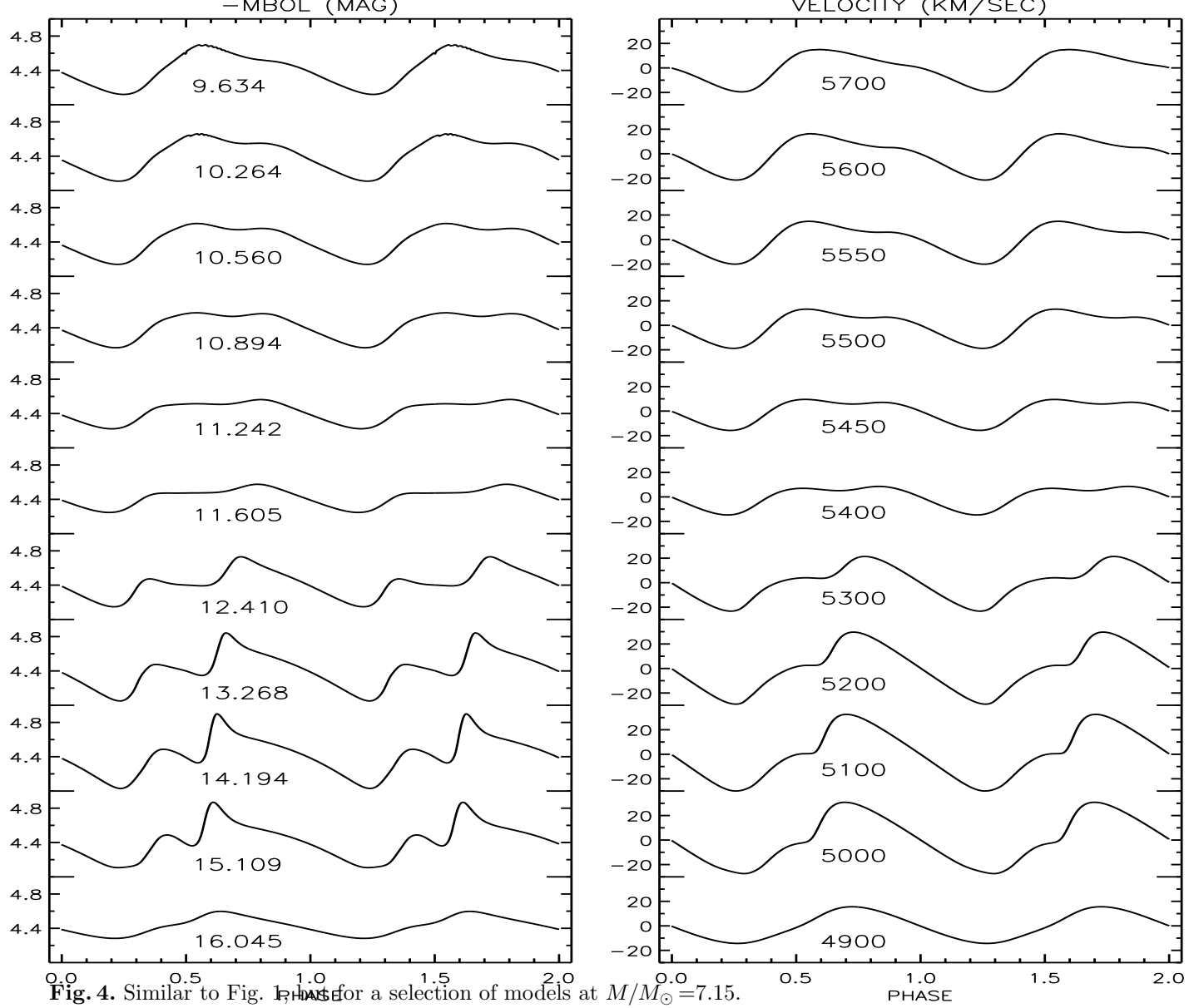


Fig. 4. Similar to Fig. 1, PHASE for a selection of models at $M/M_{\odot} = 7.15$.

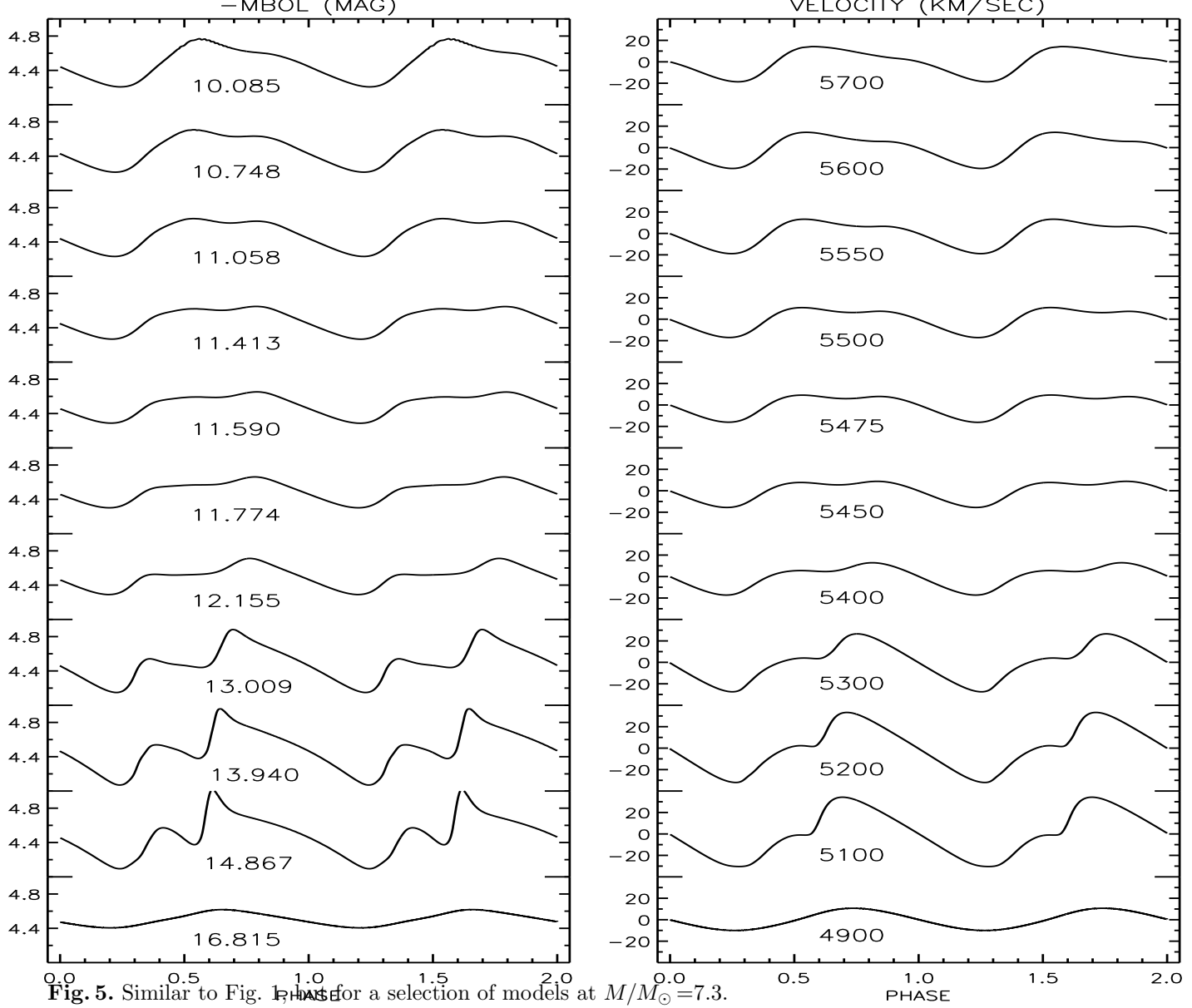


Fig. 5. Similar to Fig. 1, but for a selection of models at $M/M_{\odot} = 7.3$.

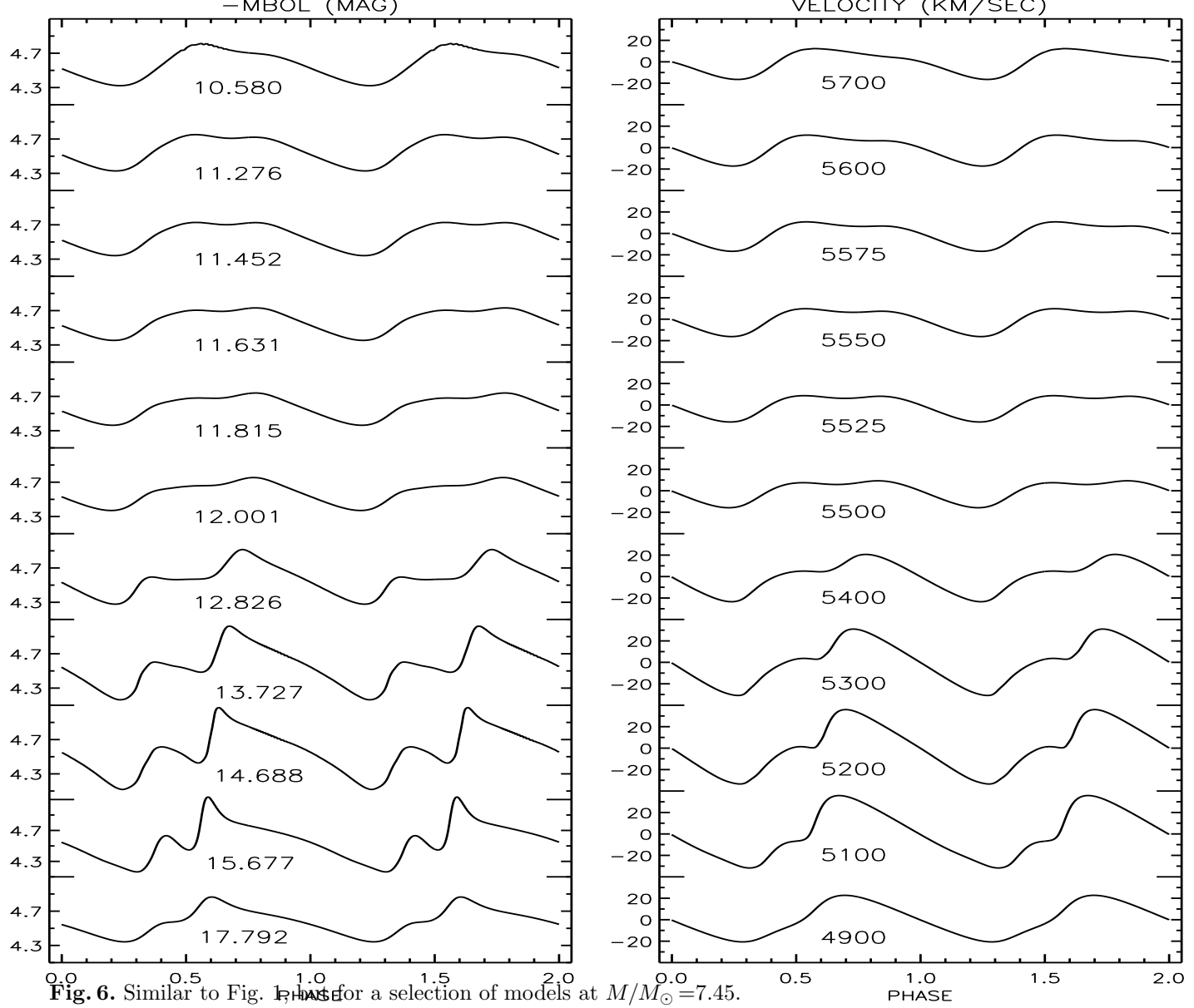


Fig. 6. Similar to Fig. 1, but for a selection of models at $M/M_{\odot} = 7.45$.

$M/M_\odot = 7$ $\log L/L_\odot = 3.65$ $TE = 5400$ K

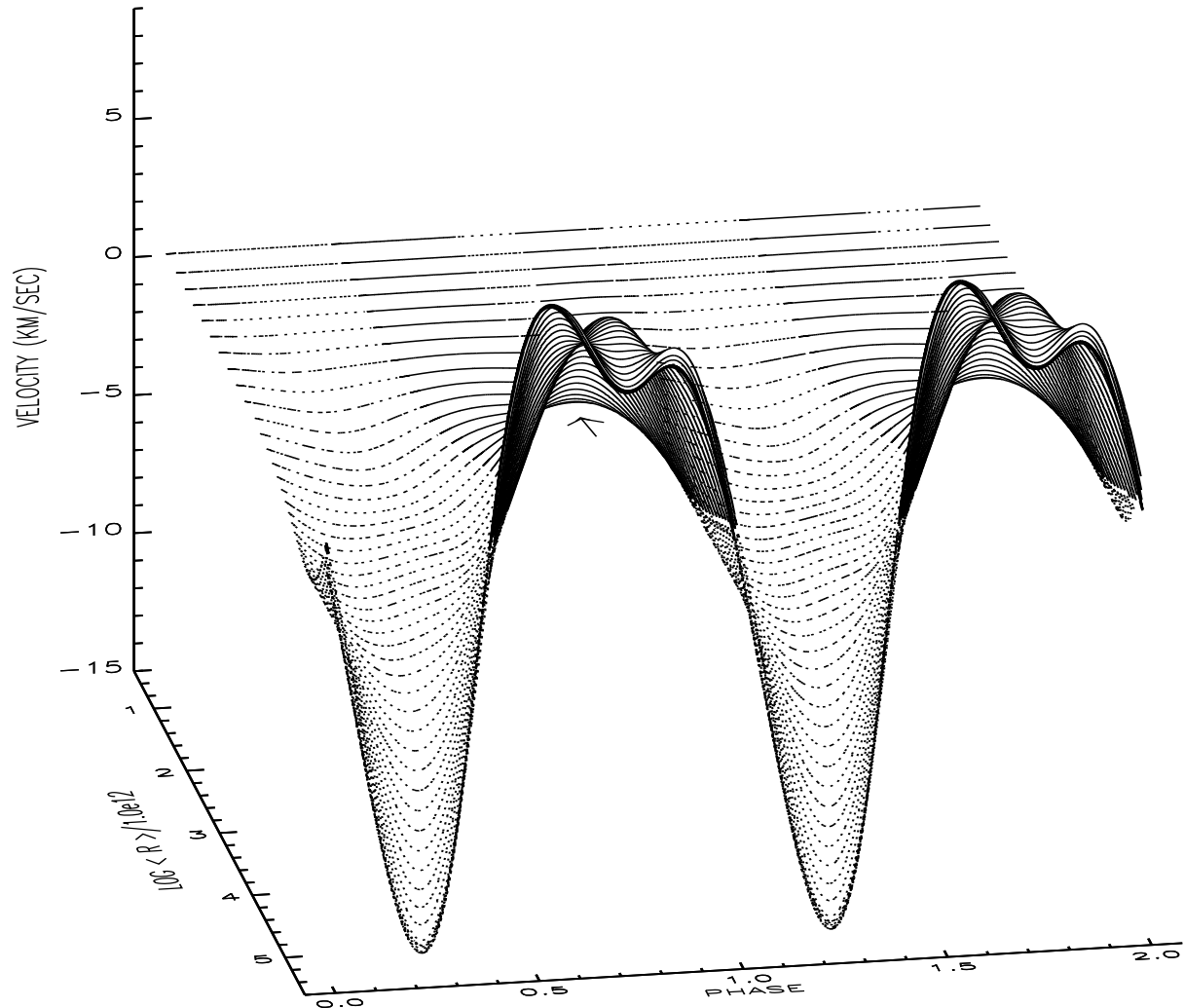


Fig. 11. Radial velocity variations as a function of mean radius and phase for the model located close to the HP center, surface at bottom. Solid and dotted line refer to positive and negative velocities. The arrow marks the interaction between inner and outer layers.

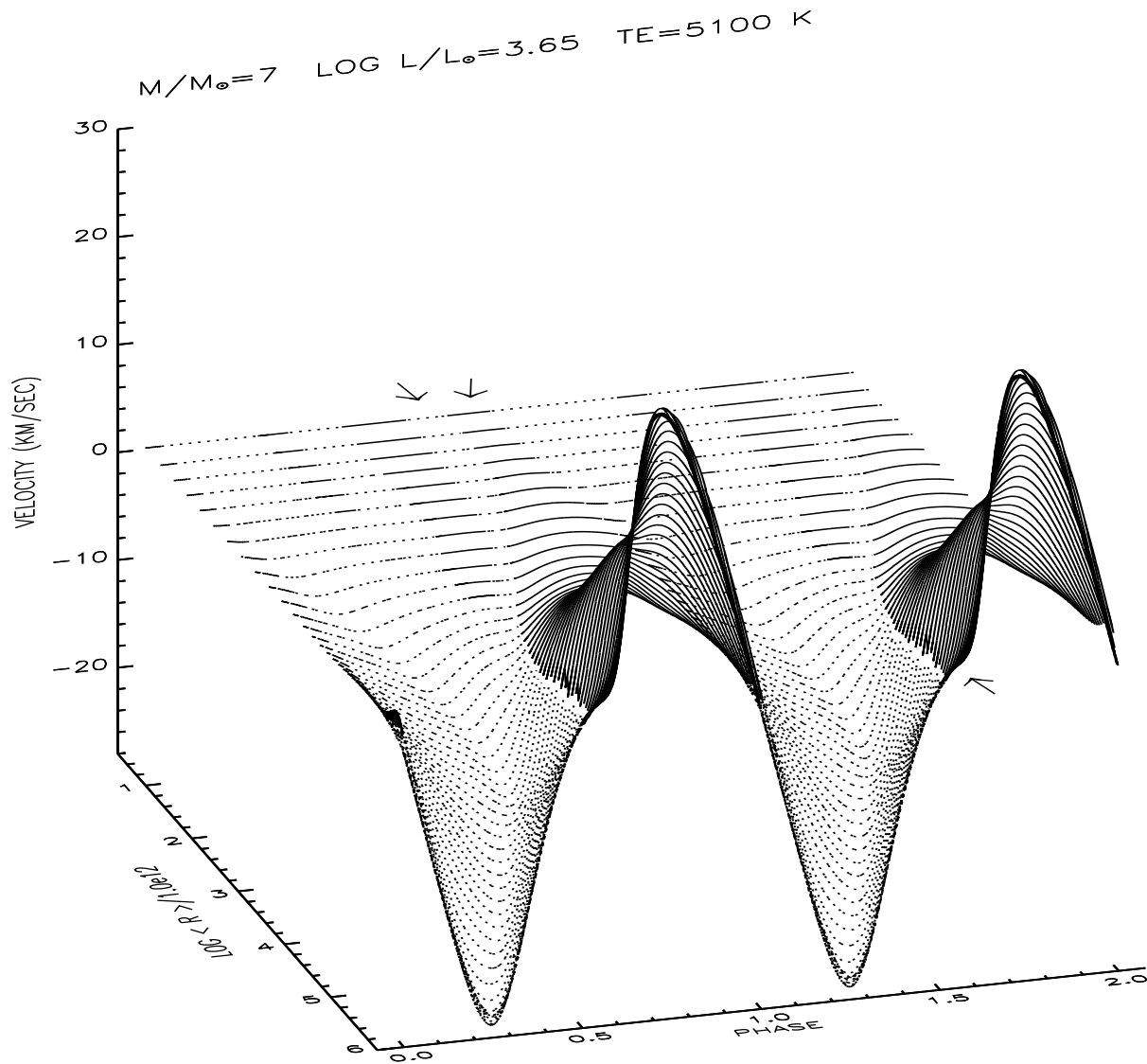


Fig. 12. Radial velocity variations as a function of mean radius and phase for a model located close to the red edge, surface at bottom. The two arrows at the base of the envelope mark the approach and the ensuing reflection of the *Christy wave* at the stellar core, while the arrow at the surface marks the phases at which appears the shoulder.

Table 1: Nonlinear Observables

M^a	$\log L^b$	T_e^c	P_0^d	$\log \bar{R}^e$	$\Delta R/R_{\text{ph}}^f$	Δu^g	ΔM_{bol}^h	$\Delta \log g_{\text{s}}^i$	$\Delta \log g_{\text{e}}^j$	ΔT^k	ΔT_e^l	KE^m
(1)	(2)	(3)	(4)	(5)	(6)	(7)	(8)	(9)	(10)	(11)	(12)	(13)
6.55	3.550	5900	6.8718	1.758	0.072	30.60	0.601	0.06	0.35	700	900	9.1320(40)
6.55	3.550	5800	7.2849	1.773	0.098	43.18	0.758	0.09	0.48	900	1100	1.5219(41)
6.55	3.550	5700	7.7306	1.789	0.102	46.07	0.714	0.09	0.51	800	1000	1.8923(41)
6.55	3.550	5600	8.2336	1.803	0.096	43.41	0.615	0.08	0.51	650	800	1.7991(41)
6.55	3.550	5500	8.7338	1.818	0.089	40.47	0.516	0.08	0.47	550	700	1.8008(41)
6.55	3.550	5400	9.2755	1.833	0.083	36.08	0.402	0.07	0.42	500	600	2.3552(41)
6.55	3.550	5300	9.8892	1.847	0.058	22.94	0.243	0.05	0.29	300	400	1.0706(41)
6.55	3.550	5250	10.2164	1.854	0.043	15.81	0.169	0.04	0.21	250	300	5.1556(40)
6.55	3.550	5200	10.5579	1.861	0.033	11.95	0.136	0.03	0.16	150	200	1.5752(40)
6.55	3.550	5150	10.9123	1.869	0.036	13.59	0.146	0.03	0.16	150	200	2.9776(39)
6.55	3.550	5100	11.2589	1.877	0.045	17.03	0.179	0.04	0.19	200	250	5.0499(39)
6.70	3.586	5900	7.2703	1.775	0.048	20.16	0.385	0.04	0.22	450	600	4.4741(40)
6.70	3.586	5800	7.7257	1.791	0.090	39.08	0.704	0.08	0.43	850	1000	1.4157(41)
6.70	3.586	5700	8.1787	1.806	0.098	43.64	0.697	0.09	0.49	800	950	1.8219(41)
6.70	3.586	5600	8.7118	1.821	0.094	42.44	0.616	0.08	0.50	700	850	3.4467(40)
6.70	3.586	5500	9.2427	1.836	0.091	40.51	0.516	0.08	0.47	600	700	2.5989(41)
6.70	3.586	5400	9.8168	1.855	0.080	33.62	0.372	0.07	0.41	450	550	2.3430(41)
6.70	3.586	5350	10.1217	1.857	0.065	25.74	0.277	0.06	0.33	350	450	1.4305(41)
6.70	3.586	5300	10.4676	1.865	0.052	19.50	0.222	0.05	0.27	300	350	8.7687(40)
6.70	3.586	5250	10.7876	1.872	0.042	15.07	0.183	0.04	0.22	200	250	3.4250(40)
6.70	3.586	5200	11.1770	1.880	0.047	18.62	0.212	0.04	0.23	250	300	1.1107(40)
6.70	3.586	5100	11.9479	1.896	0.076	29.47	0.327	0.07	0.32	400	500	2.5620(40)
6.85	3.620	5800	8.1429	1.808	0.084	35.63	0.656	0.07	0.39	750	950	1.2515(41)
6.85	3.620	5700	8.6411	1.823	0.094	41.36	0.679	0.08	0.48	750	950	1.2991(41)
6.85	3.620	5600	9.1850	1.838	0.094	41.82	0.611	0.08	0.49	700	850	1.8822(41)
6.85	3.620	5500	9.7459	1.853	0.093	40.36	0.517	0.08	0.48	600	750	3.1404(41)
6.85	3.620	5450	10.0558	1.860	0.086	36.20	0.430	0.08	0.44	500	650	2.7778(41)
6.85	3.620	5400	10.3578	1.867	0.076	30.85	0.347	0.07	0.40	450	550	2.2254(41)
6.85	3.620	5350	10.6894	1.875	0.061	23.11	0.276	0.05	0.32	350	400	1.3148(41)
6.85	3.620	5300	11.0408	1.882	0.052	17.97	0.232	0.04	0.27	250	300	6.0248(40)
6.85	3.620	5250	11.4360	1.889	0.055	22.05	0.265	0.05	0.29	300	350	2.2124(40)
6.85	3.620	5200	11.8202	1.898	0.077	32.79	0.385	0.07	0.39	450	550	2.3564(40)
6.85	3.620	5100	12.6365	1.916	0.112	44.79	0.544	0.10	0.53	650	800	7.7163(40)
7.15	3.690	5800	9.0744	1.842	0.060	24.48	0.453	0.05	0.27	550	650	3.9501(40)
7.15	3.690	5700	9.6344	1.858	0.081	34.50	0.576	0.07	0.41	700	850	5.9840(40)
7.15	3.690	5600	10.2641	1.873	0.090	37.74	0.550	0.08	0.46	650	800	2.4011(41)
7.15	3.690	5550	10.5597	1.880	0.085	34.96	0.476	0.07	0.44	550	700	2.3934(41)
7.15	3.690	5500	10.8941	1.887	0.081	31.94	0.407	0.07	0.43	500	600	2.2713(41)
7.15	3.690	5450	11.2419	1.895	0.068	25.25	0.340	0.06	0.36	350	450	1.4116(41)
7.15	3.690	5400	11.6051	1.902	0.063	23.24	0.327	0.05	0.34	350	400	8.6794(40)
7.15	3.690	5350	11.9971	1.910	0.074	30.24	0.400	0.06	0.39	450	550	3.7647(40)
7.15	3.690	5300	12.4099	1.919	0.103	44.55	0.581	0.09	0.53	650	800	7.2956(40)
7.15	3.690	5200	13.2676	1.938	0.142	58.72	0.789	0.12	0.74	900	1150	1.7414(41)
7.15	3.690	5100	14.1940	1.955	0.163	62.48	0.865	0.14	0.83	1050	1250	2.4528(41)
7.15	3.690	5000	15.1090	1.970	0.166	58.15	0.758	0.15	0.77	950	1150	3.2418(41)
7.15	3.690	4900	16.0454	1.980	0.094	29.91	0.314	0.08	0.35	400	500	1.0253(41)

Table 1: Continued

M^a	$\log L^b$	T_e^c	P_0^d	$\log \bar{R}^e$	$\Delta R/R_{\text{ph}}^f$	Δu^g	ΔM_{bol}^h	$\Delta \log g_s^i$	$\Delta \log g_e^j$	ΔT^k	ΔT_e^l	KE^m
(1)	(2)	(3)	(4)	(5)	(6)	(7)	(8)	(9)	(10)	(11)	(12)	(13)
7.30	3.720	5800	9.4996	1.857	0.048	19.32	0.358	0.04	0.21	450	550	2.5048(40)
7.30	3.720	5700	10.0848	1.872	0.071	32.81	0.560	0.07	0.40	650	800	8.2223(40)
7.30	3.720	5600	10.7479	1.888	0.083	33.67	0.493	0.07	0.43	600	700	1.9504(41)
7.30	3.720	5575	10.8600	1.891	0.084	33.78	0.480	0.07	0.44	550	700	2.1880(41)
7.30	3.720	5550	11.0578	1.895	0.081	32.06	0.440	0.07	0.43	500	650	2.1052(41)
7.30	3.720	5525	11.2599	1.899	0.078	30.04	0.397	0.07	0.41	500	600	1.9245(41)
7.30	3.720	5500	11.4131	1.903	0.074	27.89	0.380	0.06	0.40	450	550	1.6865(41)
7.30	3.720	5475	11.5898	1.906	0.070	25.31	0.363	0.06	0.38	400	450	1.3366(41)
7.30	3.720	5450	11.7741	1.910	0.067	24.35	0.359	0.06	0.36	350	450	9.9195(40)
7.30	3.720	5400	12.1549	1.918	0.075	30.11	0.420	0.07	0.40	450	550	5.4813(40)
7.30	3.720	5300	13.0085	1.936	0.126	53.97	0.731	0.11	0.65	800	1000	1.3798(41)
7.30	3.720	5200	13.9396	1.955	0.160	65.25	0.885	0.14	0.84	1050	1250	2.5421(41)
7.30	3.720	5100	14.8666	1.971	0.176	64.60	0.917	0.15	0.89	1100	1350	3.3421(41)
7.30	3.720	5000	15.8518	1.987	0.184	64.19	0.879	0.16	0.87	1100	1350	5.2853(41)
7.30	3.720	4900	16.8146	1.994	0.067	20.71	0.212	0.06	0.24	300	350	4.9524(40)
7.45	3.752	5800	9.9895	1.872	0.018	7.58	0.142	0.02	0.08	150	200	7.0975(39)
7.45	3.752	5700	10.5798	1.888	0.071	28.74	0.489	0.06	0.36	600	700	6.9298(40)
7.45	3.752	5625	11.1041	1.900	0.075	29.46	0.446	0.07	0.39	550	650	1.3650(41)
7.45	3.752	5600	11.2759	1.903	0.075	28.84	0.422	0.06	0.39	500	650	1.4235(41)
7.45	3.752	5575	11.4520	1.907	0.073	27.43	0.386	0.06	0.38	450	600	1.3788(41)
7.45	3.752	5550	11.6314	1.911	0.071	25.98	0.378	0.06	0.37	450	550	1.2519(41)
7.45	3.752	5525	11.8146	1.914	0.069	24.52	0.375	0.06	0.37	400	500	1.0727(41)
7.45	3.752	5500	12.0010	1.919	0.069	25.09	0.383	0.06	0.37	400	500	8.3532(40)
7.45	3.752	5450	12.4169	1.927	0.079	31.69	0.464	0.07	0.42	500	600	5.5981(40)
7.45	3.752	5400	12.8257	1.936	0.105	44.08	0.634	0.09	0.54	700	850	8.6258(40)
7.45	3.752	5300	13.7265	1.955	0.148	61.86	0.855	0.13	0.76	1000	1200	2.3433(41)
7.45	3.752	5200	14.6879	1.972	0.174	69.28	0.951	0.15	0.93	1100	1400	3.6237(41)
7.45	3.752	5100	15.6774	1.990	0.196	71.38	1.011	0.17	1.01	1250	1500	5.4076(41)
7.45	3.752	5000	16.7485	2.005	0.196	67.49	0.964	0.17	0.91	1150	1400	7.9229(41)
7.45	3.752	4900	17.7920	2.015	0.136	43.37	0.520	0.12	0.52	650	800	2.7150(41)

^a Stellar mass (solar units). ^b Logarithmic luminosity (solar units). ^c Effective temperature (K). ^d Fundamental period (day). ^e Logarithmic mean radius (solar units). ^f Fractional radius variation. ^g Radial velocity amplitude (Kms⁻¹). ^h Bolometric amplitude (mag). ⁱ Amplitude of logarithmic static gravity. ^j Amplitude of logarithmic effective gravity. ^k Surface temperature variation (K). ^l Effective temperature variation (K). ^m Total kinetic energy (erg).

Table 2: HP Systematic Behavior

M^a (1)	T_e^b (2)	P_2/P_0^c (3)	$A(V)^d$ (4)	$Ac(M_V)^e$ (5)	$Sk(M_V)^f$ (6)	$Ac(V_R)^g$ (7)	$Sk(V_R)^h$ (8)
6.55	5900	0.539	0.735	2.378 ⁱ	1.387 ⁱ	2.058 ⁱ	0.923 ⁱ
6.55	5800	0.537	0.944	2.717	1.123	2.953	0.852
6.55	5700	0.533	0.905	2.559	0.721	2.717	0.789
6.55	5600	0.528	0.794	2.021	0.475	2.378	0.600
6.55	5500	0.526	0.682	1.755	0.453	1.976	0.572
6.55	5400	0.525	0.551	1.976	0.460	2.021	0.605
6.55	5300	0.522	0.350	2.759	0.481	2.021	0.592
6.55	5250	0.520	0.244	2.774	0.468	1.915	0.550
6.55	5200	0.517	0.187	0.546	0.471	0.650	0.543
6.55	5150	0.514	0.210	0.587	0.548	0.681	0.706
6.55	5100	0.514	0.265	0.647	0.618	0.730	0.862
6.70	5900	0.535	0.476	1.924	1.222	1.710	0.945
6.70	5800	0.532	0.879	2.774	1.150	2.663	0.828
6.70	5700	0.530	0.886	2.390	0.689	2.584	0.739
6.70	5600	0.525	0.797	1.959	0.508	2.268	0.577
6.70	5500	0.523	0.687	1.915	0.490	2.077	0.582
6.70	5400	0.522	0.514	2.165	0.479	2.155	0.600
6.70	5350	0.524	0.393	2.802	0.473	2.096	0.582
6.70	5300	0.519	0.299	2.846	0.460	2.067	0.538
6.70	5250	0.518	0.248	0.538	0.473	0.629	0.515
6.70	5200	0.515	0.299	0.608	0.527	0.658	0.615
6.70	5100	0.510	0.485	0.818	0.681	0.818	0.965
6.85	5800	0.530	0.819	2.484	1.141	2.677	0.815
6.85	5700	0.525	0.864	2.279	0.704	2.496	0.647
6.85	5600	0.523	0.795	2.021	0.550	2.247	0.580
6.85	5500	0.522	0.690	2.003	0.517	2.236	0.585
6.85	5450	0.520	0.583	2.067	0.501	2.247	0.590
6.85	5400	0.521	0.473	2.289	0.479	2.257	0.575
6.85	5350	0.518	0.362	0.585	0.466	2.185	0.531
6.85	5300	0.516	0.311	0.580	0.481	0.626	0.497
6.85	5250	0.513	0.367	0.647	0.527	0.664	0.577
6.85	5200	0.511	0.547	0.773	0.577	0.761	0.718
6.85	5100	0.506	0.804	1.075	0.727	0.972	1.024
7.00	5800	0.528	0.713	2.110	1.078	2.365	0.801
7.00	5700	0.525	0.829	2.154	0.733	2.437	0.621
7.00	5600	0.522	0.777	1.985	0.587	2.279	0.580
7.00	5500	0.524	0.622	2.096	0.536	2.311	0.587
7.00	5450	0.515	0.517	2.030	0.499	2.333	0.567
7.00	5400	0.516	0.388	0.597	0.486	2.205	0.524
7.00	5350	0.513	0.375	0.613	0.501	0.631	0.488
7.00	5300	0.513	0.446	0.675	0.536	0.681	0.577
7.00	5200	0.507	0.858	1.042	0.885	0.939	0.866
7.00	5100	0.502	1.065	1.317	0.959	1.113	1.072
7.00	5000	0.500	0.868	1.278	0.977	1.189	1.257

Table 2: Continued

M^a (1)	T_e^b (2)	P_2/P_0^c (3)	$A(V)^d$ (4)	$Ac(M_V)^e$ (5)	$Sk(M_V)^f$ (6)	$Ac(V_R)^g$ (7)	$Sk(V_R)^h$ (8)
7.15	5800	0.525	0.568	1.809	1.024	1.994	0.792
7.15	5700	0.522	0.738	2.215	0.754	2.195	0.626
7.15	5600	0.518	0.720	2.086	0.631	2.378	0.590
7.15	5550	0.517	0.631	2.077	0.585	2.356	0.582
7.15	5500	0.517	0.546	1.994	0.534	2.401	0.560
7.15	5450	0.514	0.445	0.645	0.508	2.333	0.515
7.15	5400	0.513	0.434	0.658	0.524	0.647	0.497
7.15	5350	0.513	0.543	0.742	0.565	0.712	0.587
7.15	5300	0.508	0.802	0.919	0.972	0.855	0.692
7.15	5200	0.502	1.130	1.299	0.965	1.114	0.927
7.15	5100	0.498	1.274	1.538	1.141	1.247	1.392
7.15	5000	0.497	1.159	1.525	1.457	1.469	1.358
7.15	4900	0.498	0.507	1.252	1.092	1.174	1.146
7.30	5800	0.524	0.449	1.577	0.996	1.747	0.802
7.30	5700	0.522	0.716	2.049	0.795	2.311	0.621
7.30	5600	0.516	0.647	2.067	0.647	2.356	0.577
7.30	5575	0.519	0.635	2.154	0.610	2.413	0.575
7.30	5550	0.516	0.585	2.067	0.587	2.413	0.558
7.30	5525	0.514	0.532	2.030	0.555	2.425	0.541
7.30	5500	0.516	0.493	0.701	0.536	2.413	0.524
7.30	5475	0.514	0.475	0.683	0.538	2.367	0.501
7.30	5450	0.513	0.471	0.678	0.543	0.653	0.495
7.30	5400	0.511	0.562	0.739	0.570	0.704	0.555
7.30	5300	0.510	1.013	1.101	1.028	0.992	0.779
7.30	5200	0.500	1.271	1.433	0.980	1.237	0.953
7.30	5100	0.495	1.351	1.611	1.299	1.404	1.427
7.30	5000	0.494	1.291	1.793	1.778	1.625	1.375
7.30	4900	0.478	0.345	1.146	1.079	1.110	1.092
7.45	5800	0.522	0.178	1.283	0.972	1.273	0.894
7.45	5700	0.530	0.628	1.994	0.789	2.215	0.618
7.45	5625	0.516	0.585	2.106	0.664	2.344	0.572
7.45	5600	0.515	0.556	2.125	0.623	2.344	0.558
7.45	5575	0.514	0.513	2.049	0.582	2.356	0.543
7.45	5550	0.513	0.487	0.727	0.560	2.356	0.522
7.45	5525	0.512	0.487	0.724	0.567	2.356	0.499
7.45	5500	0.511	0.500	0.733	0.580	0.667	0.504
7.45	5450	0.508	0.616	0.782	0.615	0.724	0.565
7.45	5400	0.507	0.854	0.923	0.631	0.852	0.653
7.45	5300	0.501	1.195	1.252	0.992	1.155	0.848
7.45	5200	0.497	1.372	1.538	1.028	1.347	1.304
7.45	5100	0.494	1.492	1.774	1.389	1.699	1.463
7.45	5000	0.489	1.419	2.378	1.740	1.770	1.381
7.45	4900	0.489	0.823	1.710	1.212	1.433	1.207

^a Stellar mass (solar units). ^b Effective temperature (K). ^c Second overtone to fundamental period ratio. ^d Visual amplitude (mag). ^e Acuteness of visual light curve. ^f Skewness of visual light curve. ^g Acuteness of radial velocity curve. ^h Skewness of radial velocity curve. ⁱ The Ac and Sk values based on light curves were estimated by adopting the magnitude scale -the maximum is the minimum value-, while the Ac and Sk values based on velocity curves were estimated by adopting the theoretical notation i.e. the maximum value is attained during the outward excursion (positive values). Both for light and velocity curves we assumed that the phase is zero at maximum.

Table 3: Input parameters and nonlinear results.

Parameter ^a (1)	SK ^b (2)	III ^c (3)
M	5.35	7.00
$\log L$	3.65	3.65
T_e	5700	5700
Y	0.29	0.25
Z	0.01	0.008
P_0	11.0398	9.1025
P_2/P_0	0.4937	0.5249
Δu	37.8	38.8
ΔM_{bol}	0.71	0.65

^a Y and Z are the helium and the metal content respectively. The other symbols and their units are the same as in Tables 1 and 2. ^b SK model.

^c Paper III model.